Bull. Disas. Prev. Res. Inst., Kyoto Univ., Vol. 44, Part 1, No. 378, March, 1994

Basic Study on the Shear Behavior of Landslides during Earthquakes

— Excess Pore Pressure Generation in the Undrained Cyclic Loading Ring Shear Tests —

By Zieaoddin SHOAEI and Kyoji SASSA

(*Manuscript received on Dec., 6, 1993, revised on Jan., 19, 1994*)

Abstract

During an earthquake, undrained cyclic loading is given to saturated soil layers in slopes because the stress change during earthquakes is rapid. For reproducing the stress condition in a slope during earthquakes, a cyclic loading ring shear apparatus had been developed in Kyoto University. For this work, the shear box of the apparatus has been improved for the tests under undrained state and for monitoring the generation of pore pressure during shear.

Catastrophic landslides are often caused in granular soils such as volcanic deposits (i. e., pumice), unindurated wind deposits (i. e., loess) and so on. In the present study, undrained cyclic loading ring shear tests were carried out using three samples: pumice taken from the Ontake landslide triggered by the 1984 Nagano-Ken-Seibu earthquake (Nagano prefecture, Japan), loess from Lishan (Xian, China), and the Toyoura standard sand (beach sand) for comparison with the former two samples.

The pumice showed a rapid increase of pore pressure after failure and fast shear motion took place; the loess exhibited a gradual pore pressure build-up during cyclic loading and reached failure under a relatively small cyclic loading stress. In order to examine the influence of seismic loading direction, two conditions in which either the seismic stress is given in an almost horizontal direction or in an almost vertical direction are reproduced in the apparatus. The horizontal seismic force is usually considered to be much more dangerous than the vertical loading. However, according to the test results of pumice and loess samples, the magnitude of loaded stress necessary to cause failure in the vertical seismic loading was almost same with that in the horizontal seismic loading. This is attributed to the variation in pore pressure generation depending on the seismic loading directions.

The test apparatus and the methods adopted in this study made it possible to assess the pore pressure generation in a saturated soil layer and its shear behavior in slopes subjected to undrained cyclic loading caused by an earthquake.

1. Introduction

The necessity to study the mechanism of catastrophic landslides triggered by earthquakes has been recognized by many landslide researchers. Most studies from a soil mechanical approach have been based on the principle of subjecting a representative soil element to the same stress-strain condition in the laboratory as would be encountered in the field, and to assess the probable field performance from the resulting behavior of the laboratory test specimens.

Reproducing the stress condition of soils in slopes during an earthquake is not easy, and

the number of researchers focusing on this aspect is very limited. However, for evaluating the dynamic behavior of soils in a horizontal ground, much effort using the conventional apparatus have been made to study liquefaction and the dynamic friction angle.

1.1 Review of previous works

Liquefaction took place on the horizontal alluvial sand deposits in the Niigata earthquake (Niigata, Japan, 1964) and other events. The stress condition under a horizontal ground surface is shown in **Fig. 1**. Before an earthquake, there is no initial shear stress on the horizontal plane (**Fig. 1(a)**). During an earthquake, the normal stress on this plane remains constant while cyclic shear stress is induced for the duration of ground shaking **Fig. 1(b)** and **(c)**. After the severe damage caused by the Niigata earthquake, the study of liquefaction has become a major focus of many investigations.

The most common experiment for liquefaction was conducted for the first time by Seed and Lee[1]. They tried to reproduce the stress condition during an earthquake by cyclic loading triaxial compression tests. As they noted, in triaxial tests, even if the axial stress increases by an amount, σ_d and simultaneously the all-around confining pressure on the specimens reduces by an equal amount, σ_d, the effect of the reduction in all-around pressure would simply reduce the pore pressure in the saturated sample by σ_d without causing any change in the effective stress in the sample. Therefore, in the real tests only the vertical stress is changed. In the triaxial tests, since the location of shear surface cannot be decided, it is neither possible to control the stress condition on a shear surface, nor to estimate the shear surface area precisely.

Seed and Peacock[2] tried to explain the stress condition during earthquake using the cyclic simple shear apparatus. From the test results, they concluded that the filed loading conditions were, in principle, correctly simulated in the laboratory. Both in the field and in the laboratory tests, the soil elements are consolidated under an effective overburden pressure and a lateral pressure. During an earthquake or cyclic loading in the laboratory, the soil element is subjected to horizontal and vertical shear stress.

Deformation of samples before and after failure in triaxial tests and simple shear tests are shown in **Fig. 2**. In triaxial tests, in addition to the encountered inaccuracy due to the unknown location of the shear surface, the area of the shear surface changes (**Fig. 2 a**)), and large deformation makes it difficult to evaluate the stress on the shear surface. For the liquefaction test, there is no problem, but, it poses a difficulty if the test is to be applied to land-

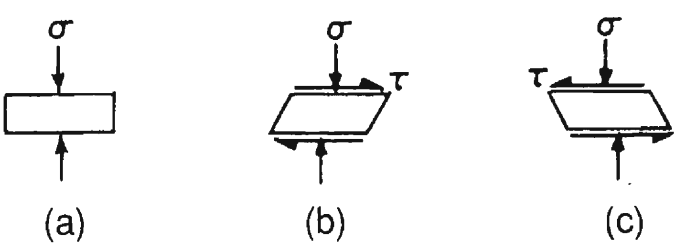

Fig. 1 Stress condition for a soil layer under horizontal ground surface before and during an earthquake.

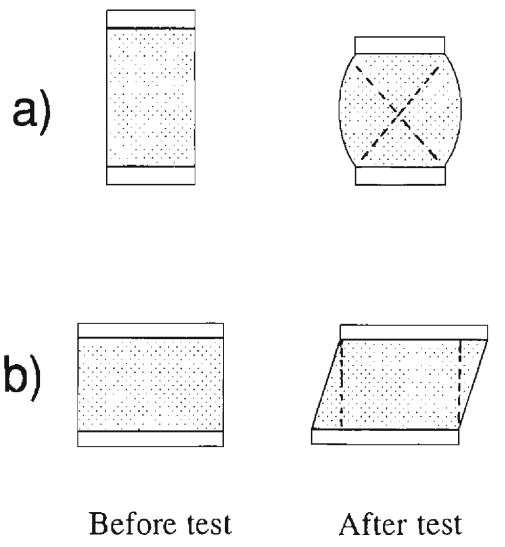

Fig. 2 **Deformation of samples in the triaxial tests a) and in the simple shear tests b).**

slides. In the simple shear test, the area of shear surface is kept constant, but when a large displacement takes place (**Fig. 2 b**)), the area on which the normal stress is loaded will decrease.

Ishihara and Yasuda[3] used a hollow cylinder triaxial apparatus for liquefaction tests. To consolidate the sample under an all-around pressure, an axial stress as well as a cell pressure in the hollow and to the outside were applied. Then a cyclic torsional shear stress (τ_d) was loaded under the undrained condition. This test does not have the shortcomings described in **Fig. 2**; the area of shear surface can be kept constant in respect to the normal stress and the shear stress. This apparatus will be appropriate for reproducing the stress conditions in slopes as well as in horizontal ground. However, tests with a very large shear displacement like in the ring shear apparatus cannot be performed due to limitations of the rubber membrane. Tests in this investigation were only focused on liquefaction under a horizontal ground.

Another important soil characteristic relating to earthquake loading is dynamic friction angle. Shibata and Yukitomo[4] used a triaxial test apparatus to carry out triaxial vibration tests for estimation dynamic friction angle of dry and saturated sands. In this method a constant magnitude of cyclic cell pressure and a gradually increasing magnitude of cyclic axial stress were applied, so that, dynamic stress change may take place along the dynamic failure line at failure and the precise dynamic friction angle may be evaluated. This work did not aim at reproducing the initial stress before an earthquake and cyclic stress during earthquakes in slopes.

For evaluating the soil characteristics at several sites of landslides that occurred during earthquakes, Ishihara[5] used a cyclic loading triaxial apparatus similar to that used by Seed and Lee[1]. However he applied an initial shear stress in his test procedure. In this method of triaxial test, isotropically consolidated specimens were first subjected to a certain level of initial

axial stress under the drained condition, and then subjected to a series of cyclic loads in the axial direction. His work aimed at studying shear strength mobilized during earthquakes.

The most important characteristic of landslides is a very long shear displacement along the sliding surface. Large displacement cannot be reproduced in triaxial tests, simple shear tests and hollow cylinder triaxial tests in which the shear displacements are only a few centimeters. In the ring shear apparatus, shear displacement as long as a real landslide is possible, which is one of the major advantages of this apparatus. Development of the ring shear apparatus was reviewed by Bishop, *et al.*[6]. Later, Lemos, *et al.*[7] tried to study the effect of earthquake loading on soil strength using a conventional ring shear apparatus. They changed the shear speed from 0.01 mm/min to 400 mm/min. They found that some soils had positive rate effect that could produce slow failure during earthquakes, whereas in one sample there was a negative rate effect that could produce fast failure.

Yatabe, *et al.*[8] investigated the residual friction angle of clayey soils from landslides that had occurred in a metamorphic region using a conventional constant-speed ring shear apparatus. They monitored pore pressure generation by inserting a stainless needle near the shear surface from the bottom.

These series of ring shear apparatuses were the same as the conventional ring shear apparatus in respect to speed control. However, to simulate the behavior of soils under cyclic loading for the mechanism of earthquake-induced landslides, cyclic shear stress loading and cyclic normal stress loading are necessary. In 1992, Sassa[9] developed a new torque-control cyclic loading ring shear apparatus for reproducing the stress condition in slopes during earthquakes. He performed a series of constant-volume cyclic loading tests employing the Ontake pumice (Ontake landslide, Nagano Prefecture, Japan 1984) to interpret the mechanism of this landslide. It was the first ring shear apparatus that was capable of shear stress control (not shear speed). He monitored pore pressure generation using needles that were inserted near the shear surface. The shear box was for drained tests, so that undrained tests were not performed.

Shoaei and Sassa[10] used the newly-developed cyclic loading ring shear apparatus for interpreting the mechanism of some landslides triggered by the 1990 Iran earthquake. In the tests of this investigation, initial normal stress was kept constant and cyclic shear stress was applied. Pore pressure was not measured, so that the dynamic friction angle in the total stress concept was examined.

1. 2 Significance and aim of this work

(1) Undrained cyclic loading tests: In a saturated state, the dynamic stress changes due to earthquakes (0.5 to 10 Hz) should correspond to the undrained loading condition, thus, resulting in pore pressure generation. To reproduce an undrained loading state in the laboratory, modification of the shear box was tried in this work and a better monitoring system of pore pressure was designed for measuring the average value of pore pressure over the whole shear surface during a long shear displacement.

(2) Reproducing seismic stress directions: Before an earthquake, a soil element in a slope is subjected to the initial shear stress τ_0 and the initial normal stress σ_0. In many cases it appears that the main forces acting on a soil element in the field during an earthquake are

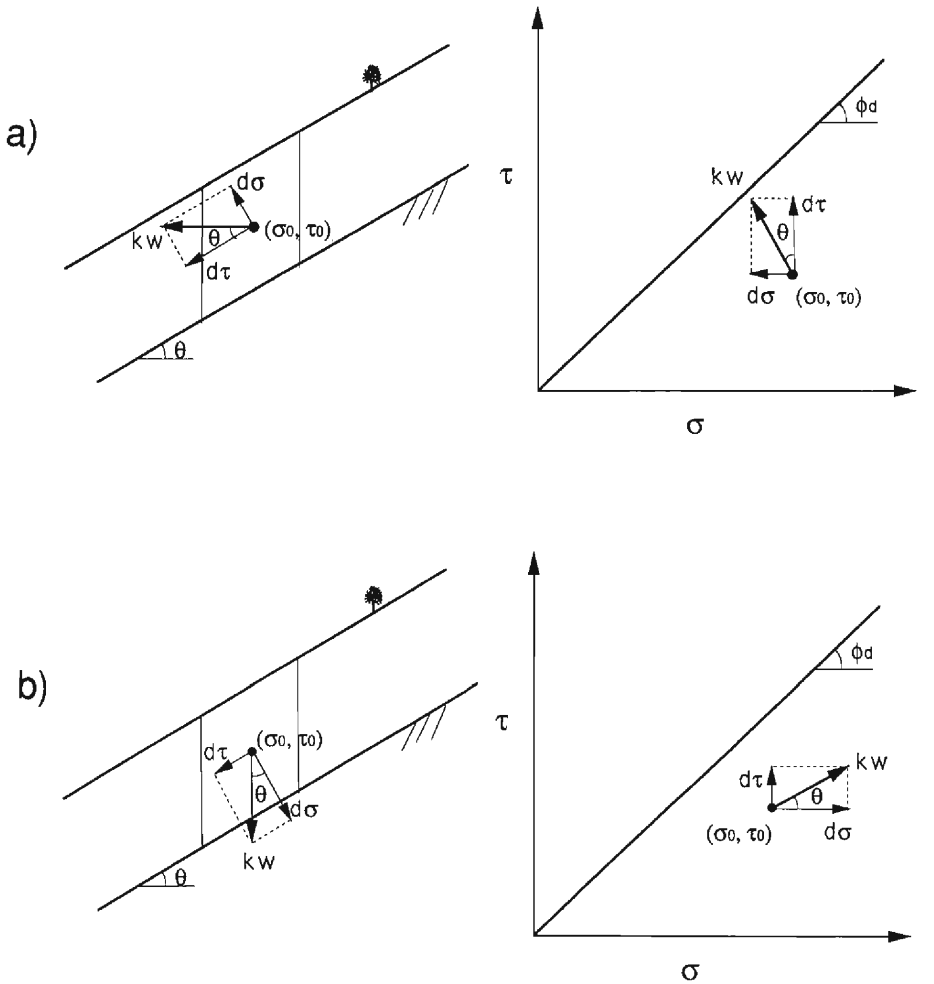

σ_0, τ_0 : Initial stress, W : Self weight of the soil column, kW : Seismic stress, $d\tau$: Increment of shear stress, $d\sigma$: Increment of normal stress, ϕ_d : Dynamic friction angle, θ : Slope angle

Fig. 3 Stress condition in the field and in the stress diagram due to the horizontal acceleration of earthquake a) and due to the vertical acceleration of earthquake b).

those resulting from the upward propagation of S–wave (shear wave) from the underlying rock formation. Such a horizontal seismic force will be superimposed on the initial shear stress τ_0 and the initial normal stress σ_0. This stress condition in the slope and in the stress diagram is shown in **Fig. 3 a)**.

Another extreme type of seismic force is vertical shaking. This can be caused, for instance, by the P–wave (dilational wave) part of a very close, strong event. This stress condition in the slope and in the stress diagram is shown in **Fig. 3 b)**.

However, during a real earthquake, the vertical force may hit the slopes first, and the horizontal force will come later, or a combination of vertical and horizontal forces may hit the slopes simultaneously. In this work, the effects of the above mentioned two types of seismic loading will be analyzed independently for simplification.

(3) Shear characteristics: Many catastrophic landslides during earthquakes occur in fully saturated granular non cohesive soils such as silty sands, pumice, loess and so on. The shear characteristics are different due to different soil textures. These different shear behaviors of soils obtained from the test results can be used for assessing the occurrence of landslides and their post-failure motion during earthquakes. For this purpose, two natural samples of pumice and loess in which the occurrence of many landslides have been reported were selected.

2. Test apparatus

2. 1 General design

Fig. 4 is a schematic diagram of the apparatus. Sample (I) is placed in the ring shear box. The outer steel cases of the shear box are provided with rectangular windows of transparent acrylic resin which makes the sample visible during the test. The lower half rotates by a servo motor (rotating parts are marked with dots in the figure), while its upper half (slightly moving parts are marked with inclined dash in the figure) is retained to the stable base through a load cell (C3) to measure shear resistance.

The front view of the apparatus is presented in **Photo 1**. The lower half of the shear box, the sample and its shear zone after shearing are shown in **Photo 2**. The inner diameter of the shear box is 21.0 cm, the outer diameter is 31.0 cm and the shear area is 408.4 cm^2. The depth of the shear box under the shearing plane is 4.0 cm, the height over the shear plane is 7.0 cm and the height of sample above the shear plane depends on the volume change during consolidation. Twelve porous disks (metal filters) are fixed to the loading plate (H) and to the base to allow drainage. Pins are fitted in the base and the loading plate in order to prevent the slipping of the two halves of the sample inside the shear box. The rubber edges (J) are affixed to the lower edges of the inner and the outer rings in order to prevent leakage of sample and water during consolidation and shearing.

2. 2 Pore pressure measuring set

The accurate measurement of pore pressure was one of the biggest problems during this work. Many attempts to measure the average value of generated pore pressure along the whole shear zone were made.

First, the measurement of pore pressure was tried by needles. For this purpose the needles with their tips covered by porous stone were inserted at pre-determined heights inside the sample from the upper part and were fixed to the upper lid. The outlets of the needles were connected to the pore pressure transducer. The result of the test was not satisfactory because of certain shortcomings in the system; 1) the area of the porous stone (covering the needle tips) was insufficient, and pore pressure measurements were delayed in the low permeable soils

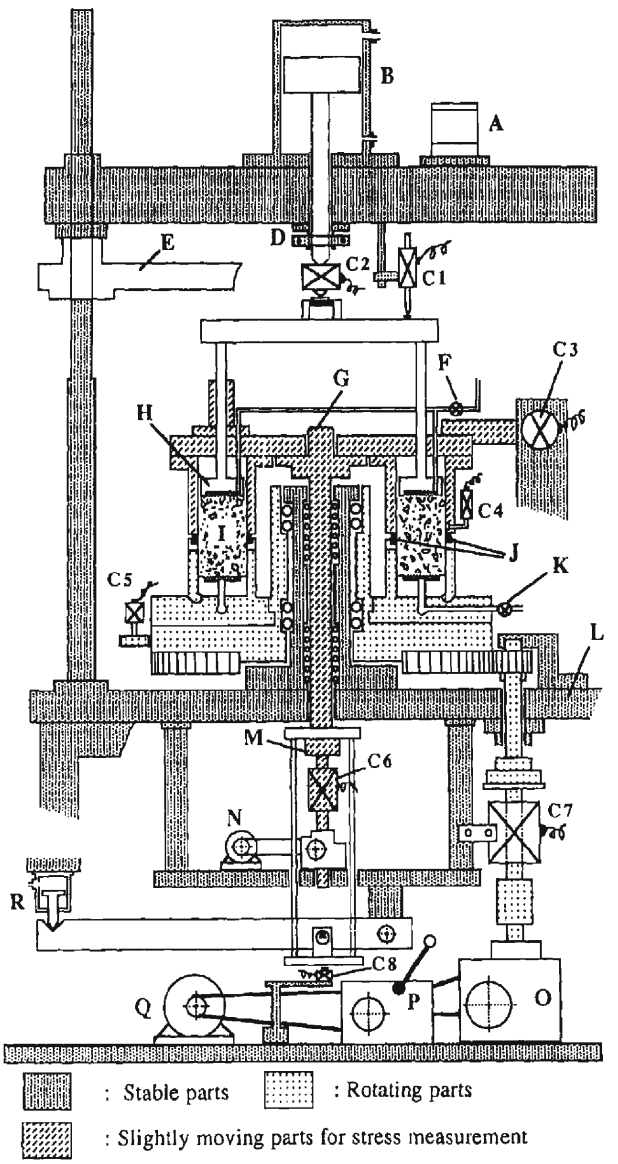

A: Lifting-crane motor, **B:** Air piston, C_1: Sample-height linear transducer, C_2: Vertical load cell (VL1), C_3: Shear resistance load cell, C_4: Pore pressure transducer, C_5: Shear displacement rotary transducer, C_6: Vertical load cell (VL2), C_7: Torque transducer, C_8: Gap sensor for gap controlling, **D:** Piston-axis stopper, **E:** Lifting arm, **F:** Upper draining valve, **G:** Central axis, **H:** Loading plate, **I:** Sample, **J:** Rubber edges, **K:** Lower draining valve, **L:** Base, **M:** Rotary joint, **N:** Gap control servo motor, **O:** Transmission gear box, **P:** Reducer gear box, **Q:** Shearing servo motor, **R:** Air piston cylinder for counter dead-weight.

Fig. 4 Schematic diagram of the undrained cyclic loading ring shear apparatus.

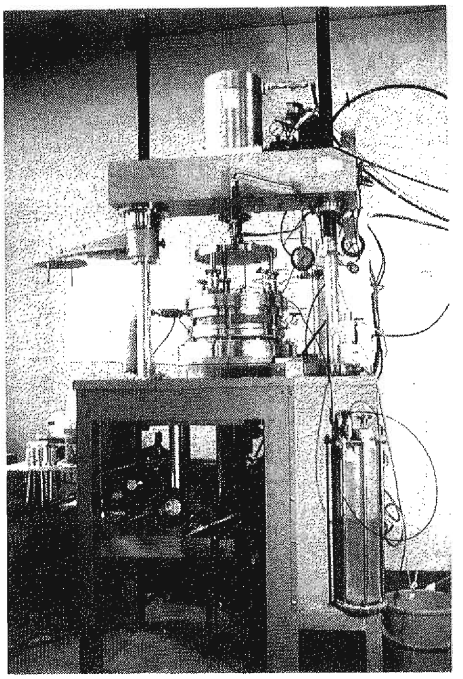

Photo 1 Frontal view of the undrained cyclic loading ring shear apparatus.

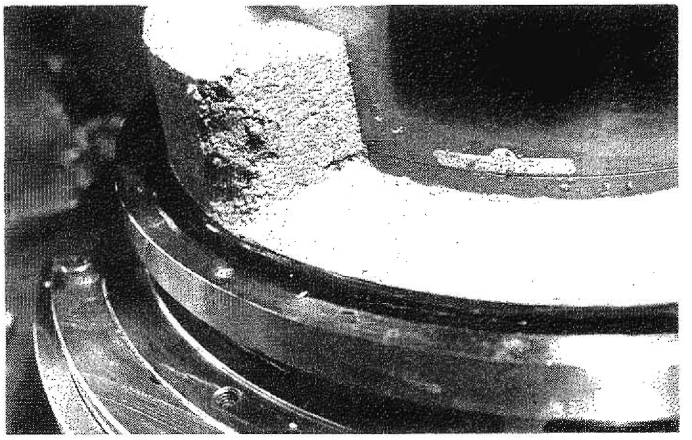

Photo 2 Lower part of the shear box and the shear zone of the pumice sample after the tests.

during rapid normal stress loading or rapid shearing. 2) the thickness of the shear zone was different for various samples, so that the prediction of the right heights of the needle tips was very difficult. In many tests, soon after the shearing started, the needles were bent and broken.

To avoid these problems, a method of pore pressure measurement by a set built on the inner ring was tried. In this method, two gutters with the dimensions of 3×3 mm and 6 cm long were built in the lower part (at the height of 2 mm above the shear plan) of the inner ring. These gutters were covered by porous stone and were connected to the pore pressure transducer by copper pipes. The result was satisfactory during consolidation of samples. However, since the porous stone surface area was still insufficient, soon after shearing started, the porous stone often became clogged by fine grains generated along the shear zone, causing appreciable error in the results. We need the average value of pore water pressure because normal stress and shear stress are measured on average over the whole shear plane, while this method only produced a local measurement, not giving the average value of generated pore pressure along the shear zone.

Finally, a method of pore pressure measurement along the whole circumference of the upper edge of the outer–upper part was designed. This method was very successful and was used for this work. As shown in **Fig. 5 a**), Pore pressure is measured at a level of 2 mm above the shear plane. The gutter (4×4 mm) along the whole circumference was built near the lower end of the outer–upper part (stable part, **Photo 3 a**)) of the shear box. Two annular metal filters with pore–sizes of 100 μm and 40 μm respectively (from inside) were placed inside the annular gutter. A felt fabric cloth was placed between these two metal filters to prevent the outside (40 μm) metal filter from becoming clogged with clay particles. The pore pressure in the shear zone was monitored by a pressure transducer (C4 in **Fig. 4**, shown in **Photo 3 b**), which was directly screwed to the elbow on the side of the outer–upper part of the sample box.

2. 3 Undrained shear box

As shown in **Fig. 5b**), the loading plate was sealed by two "O" rings. To prevent leakage from the gap between the two halves of the sample box, the optimum elasticity of rubber edges is necessary, which proved to be 45° (Rubber Hardness Index, 45° JIS). Rubber edges of 7 mm thickness were affixed to the lower rings (**Photo 2**). For a higher contact stress, the surface of the rubber edges facing the stainless steel of the upper halves were cut in stair–shape, and constantly pressed under 100 kgf. These edges were, thus, able to maintain the undrained state under 3.0 kgf/cm^2 water pressure. The surface of the rubber edges were coated by Teflon spray in order to reduce friction. Drainage was allowed by keeping the upper and lower valves (F and K in **Fig. 4**) open during consolidation and draining tests. The undrained condition was maintained by keeping the two valves closed.

The extent to which the undrained condition of the shear box is maintained was checked as follows : any air in the water path on the base of the sample box was initially removed. The upper lid of the sample box was then fixed and the sample box was filled with de–aired water. Next, the air from upper drainage path was also removed. After closing the drainage valves, the water was loaded to the level of 2.9 kgf/cm^2 of normal stress. At this stage, the loading

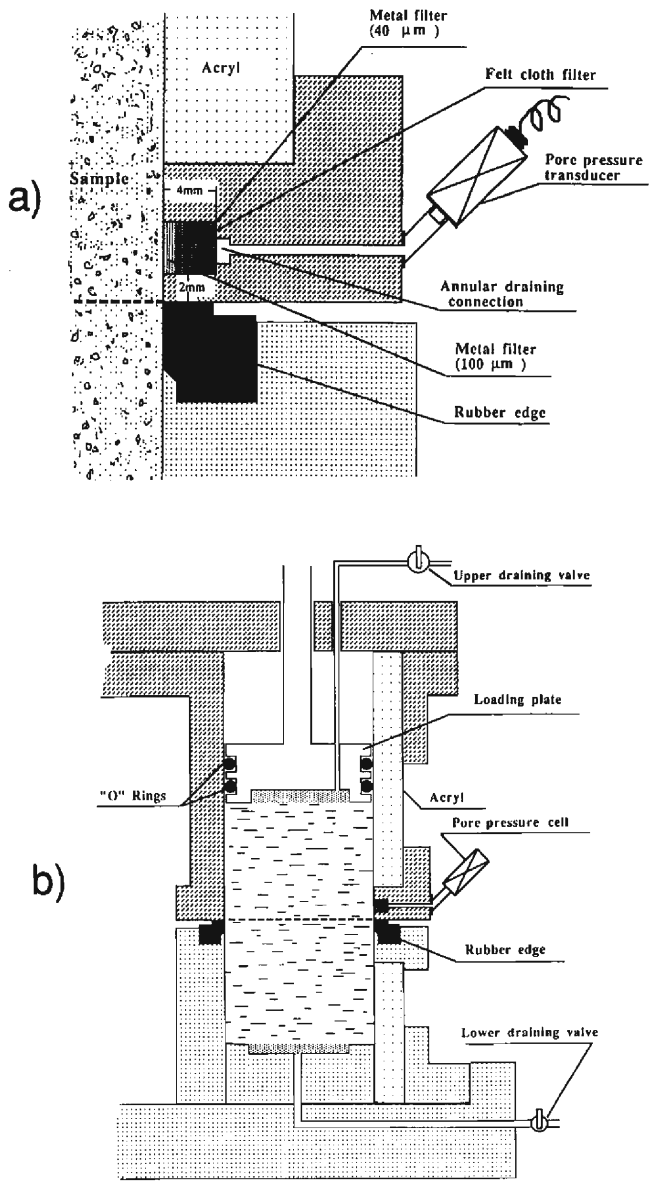

Fig. 5 Structure of the pore pressure monitoring system a) and the undrained shear box b) (section of half part).

axis of the air piston was locked by a stopper (D in **Fig. 4**). The position of the loading plate was then fixed. Due to the position of C2 load cell in **Fig. 4**, any small amount of water leakage should result in a high decrease in the values of normal stress and water pressure. Then the shearing with shear velocity of 30 cm/sec was applied. **Fig. 6** is a result of this test. During 54 m of shearing, neither the level of the normal stress nor the water pressure changed,

a)

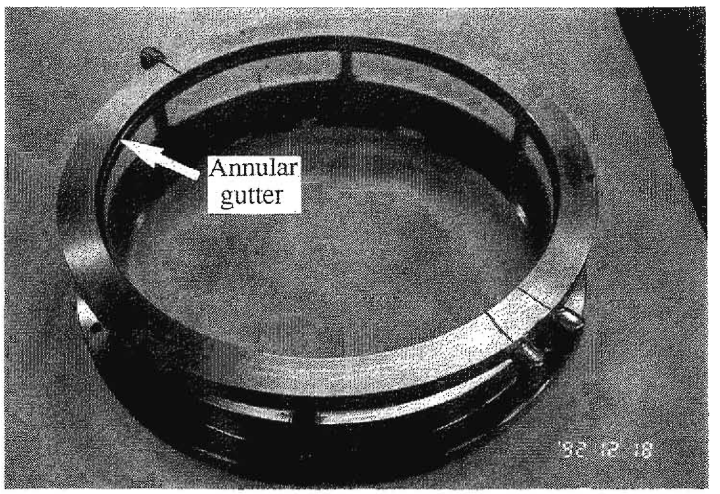

b)

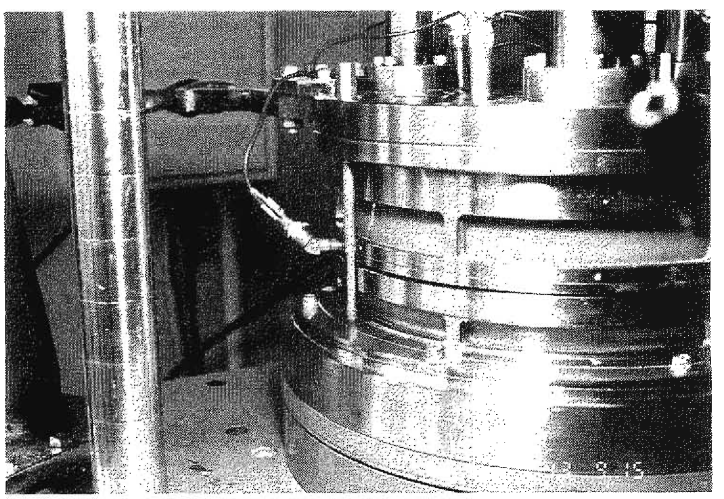

Photo 3 Annular gutter in the upper ring a) and pore pressure transducer shown at the left side b).

which confirmed that no leakage occurred during high speed shearing and the undrained condition was successfully achieved.

The normal stress loading system, shear stress loading system, gap control system and also calculations of normal stress, shear stress and shear resistance are presented in the **Appendix**.

2. 4 Characteristics of the undrained cyclic loading ring shear apparatus

The major characteristics of the apparatus used in this study are summarized below :

(1) The position of shear plane is pre-decided and a clear shear plane is formed inside the sample which is not the case in triaxial tests. This plane can be considered as a potential sliding surface in the field. The initial stress condition of the normal stress and the shear

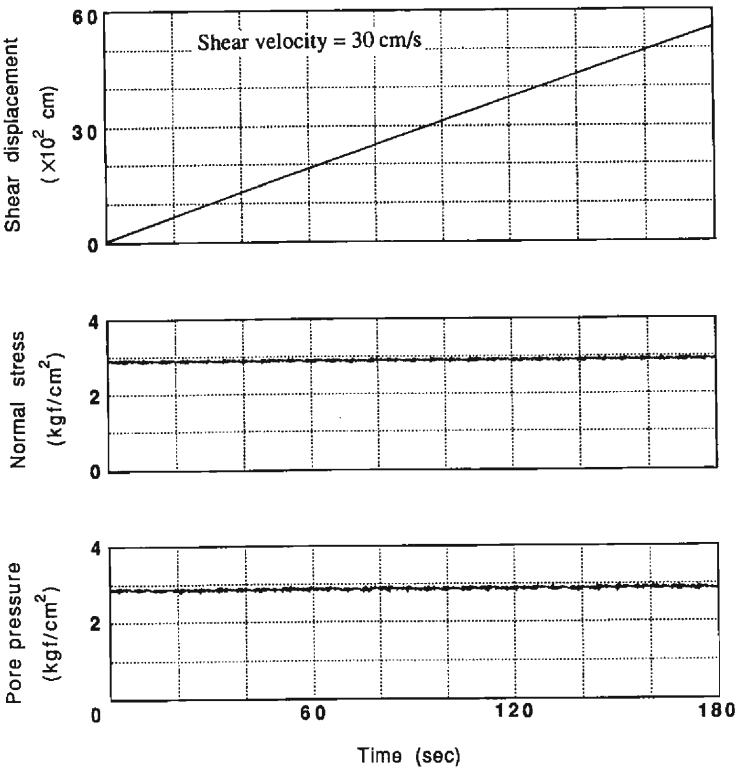

Fig. 6 The result of the test for checking the undraining precision of the shear box during shear.

stress can be applied to this pre-decided plane in order to reproduce the initial stress condition in the field before an earthquake (Fig. 7).

(2) Both initial normal stress and initial shear stress are applied by using an air servo valve and a servo motor, both operated through a personal computer and two servo amplifiers. Feedback signals from the relative load cell and transducer are sent to the servo amplifiers, so that the level of stress during consolidation, initial shear stress loading and cyclic loading can be automatically controlled. After attaining the initial stress level, the cyclic loads of the normal stress and the shear stress can be superimposed on this initial stress using the servo control system. The number of cycles, phase difference between the cyclic shear and cyclic normal stress and the amplitude of cyclic loading can be controlled so as to reproduce different stress conditions in the slopes during actual earthquakes.

(3) The development of undrained shear box together with the measurement of pore pressure along the shear zone makes this apparatus capable of studying the role of effective stress as well as the total stress on the slope stability during an earthquake.

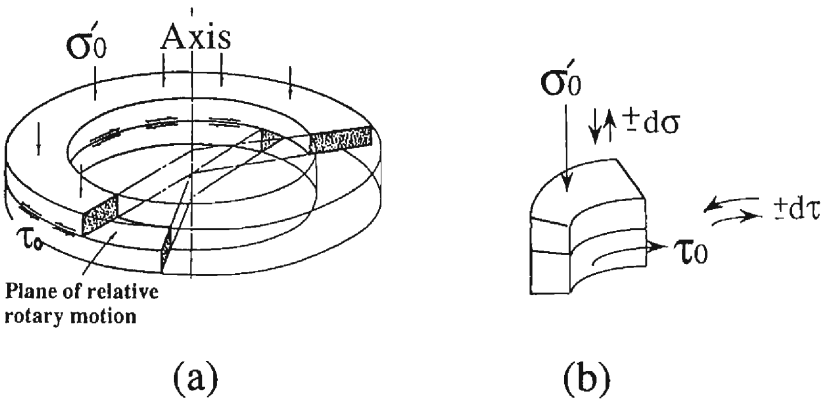

Fig. 7 Ring shear test sample (a) and a soil element under cyclic loading in the cyclic loading ring shear apparatus (b).

3. Samples and test procedure

3.1 Samples

As mentioned above, many catastrophic landslides during earthquakes occur in fully saturated granular non cohesive soils such as pumice, loess, silty sands and so on. Due to the difference in grain-size distribution and grain texture, the mechanism of pore pressure generation and shear behavior of soils are different. For this study three samples were selected.

(1) **Pumice**: This sample was collected from the source area of the Ontake landslide triggered by the 1984 Nagano-Ken-Seibu earthquake. The sample was composed of medium to coarse grains. The grain-size distribution plot of this sample is shown in **Fig. 8**. The pumice grains are normally granular aggregates with rough surfaces that are characterized by high interlocking.

(2) **Loess**: This sample is a typical Chinese loess that was collected from Lishan (Xian-China). The grain-size distribution of this sample, mainly composed of fine grains, is shown in **Fig. 8**.

(3) **Toyoura standard sand**: The grain-size distribution of the sample of so called Toyoura standard sand (beach sand) is shown in **Fig. 8**. It is mainly composed of medium grains with low susceptibility to grain crushing during shearing. Some physical properties of the samples employed are shown in **Table 1**.

The dynamic friction angles for these samples were determined in accordance with the Mohr-Coulomb law for non cohesive sample.

$$\tau_f = \sigma \tan \phi_d \qquad (3\text{-}1)$$

where τ_f: shear stress at failure, σ: normal stress, ϕ_d: dynamic friction angle. The failure line for each test was drawn by considering the values of τ_f and σ when a relatively large shear displacement started.

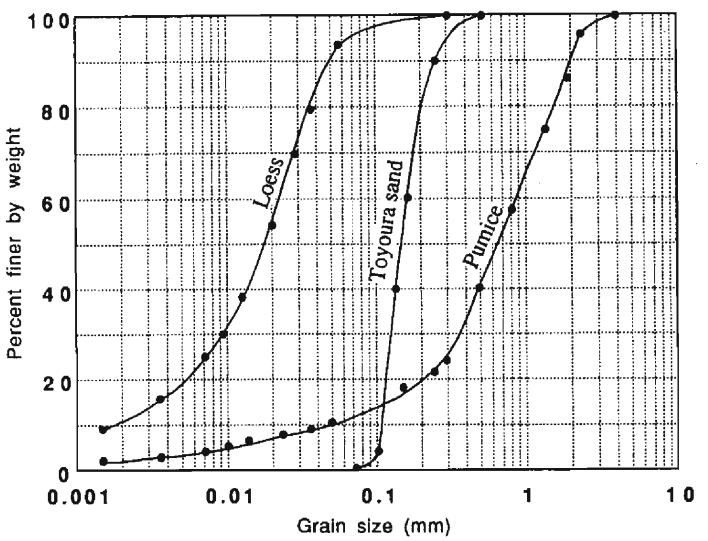

Fig. 8 Grain–size distribution of pumice, Toyoura sand and loess samples.

Table 1 Some physical properties of the employed samples and B_D value of each test measured after consolidation.

Samle	Test No.	G_s	γ_d (Field)	γ_d (Test)	k (cm/s)	e	B_D
Toyoura sand	T–Sand–1	2.64	—	1.48	3.3×10^{-2}	0.78	0.97
	T–Sand–2	2.64	—	1.48	3.3×10^{-2}	0.78	0.98
Pumice	Pumice–1	2.67	0.70	0.70	2.5×10^{-3}	2.81	0.98
	Pumice–2	2.67	0.70	0.71	3.3×10^{-3}	2.76	0.96
Loess	Loess–1	2.71	1.51	1.58	7.0×10^{-5}	0.79	0.98
	Loess–2	2.71	1.51	1.59	7.0×10^{-5}	0.79	0.97

G_s : Specific gravity, γ_d : Dry unit weight (gf/cm^3). k : Coefficient of permeability, e : Void ratio, B_D : Pore–pressure parameter.

3. 2 Test procedure

(1) Selection of test mode :

(a) Undrained condition : Due to relatively high–frequency seismic loading (0.5–10 Hz), saturated granular soils in slopes during an earthquake are usually in the undrained state. Therefore, all tests were carried out using saturated samples under undrained condition. All cyclic loading tests were carried out after confirming the B_D value (pore pressure parameter in the undrained direct shear state) to be greater than 0.95 before loading cyclic stress.

(b) Frequency : The frequency of strong earthquake tremors ranges from 0.5 to 10 Hz. Published conclusions on the effect of frequency are various. Peacock and Seed[11] showed that varying the frequency of stress cycles from 1/6 to 4 Hz produced little effect on the number of cycles causing liquefaction in sands in the simple shear test. Sand, being a relative-

ly permeable material, relying on no obviously time-dependent loading, might be expected to show little sensitivity to the rate of loading. Brown, *et al.*[12] stated that varying the frequency in the range 0.01 to 10 Hz has no significant effect on cyclic triaxial test results for Keuper marl (plasticity index $\sim$ 26). Pande and Zienkiewicz[13] reviewed previous researches on the effect of frequency on soil strength and concluded that the effect of frequency on soil strength is greater for more plastic clays. Thus, it can be concluded that in non-plastic or low-plastic material the strain process is frequency-independent.

In this work, for accurate measurement of pore pressure and also for accurate control of cyclic stress, a low-frequency cyclic loading test was necessary. Since the employed samples were non plastic, a frequency of 0.1 Hz was used for cyclic loading tests.

(c) Cyclic loading: Preliminary tests showed that the residual pore pressure did not build-up during cyclic loading in the Toyoura sand and pumice. Therefore, to obtain the amplitude of the loaded stress necessary to cause failure, a stepwise increase of the cyclic stress was applied. However, the loess sample, exhibiting a gradual pore pressure build-up was subjected to a constant amplitude cyclic stress.

(d) Loading direction: A slope angle (sliding surface angle) of 30° was considered for this study because this value is the most probable round number for earthquake-induced landslides. The relative amplitudes and phases of cyclic normal stress and cyclic shear stress were selected in order to simulate the resultant of cyclically loaded stress direction in vertical and horizontal tremors. These stress conditions in the field and in the stress diagram are illustrated in **Figs. 3 a)** and **b)**.

(e) Loading type A: In this type of test, the cyclic shear stress and the cyclic normal stress were loaded to simulate the state of vertical seismic loading in slopes (**Fig. 3 b)**). The test program of applied sinusoidal stresses versus time plot is shown in **Fig. 9 a)**:

$$\sigma=\sigma_0\pm d\sigma=\sigma_0\pm kW\cos\theta\sin\omega t \tag{3-2}$$

$$\tau=\tau_0\pm d\tau=\tau_0\pm kW\sin\theta\sin\omega t \tag{3-3}$$

where $d\sigma$: increment of normal stress, kW: Seismic stress, θ: Slope angle (30° in this work), ω: angular velocity, σ: normal stress at any given stage, σ_0: initial normal stress, $d\tau$: increment of shear stress, τ: shear stress at any given stage, τ_0: initial shear stress.

(f) Loading type B: In this type of test, the cyclic shear stress and the cyclic normal stress were loaded to simulate the state of horizontal seismic loading in slopes (**Fig. 3 a)**). The test program of applied sinusoidal stresses versus time plot is shown in **Fig. 9 b)**:

$$\sigma=\sigma_0\pm d\sigma=\sigma_0\pm kW\cos\theta\sin\omega t \tag{3-4}$$

$$\tau=\tau_0\pm d\tau=\tau_0\pm kW\cos\theta\sin(\omega t+\pi) \tag{3-5}$$

(2) Sample preparation: Pumice and loess in the Quaternary deposits usually are not overconsolidated and undisturbed sampling is not possible for the ring shear test. Therefore, the disturbed samples were used so as to produce a normally consolidated state. The degree of saturation having a great effect on the generation of pore water pressure, full saturation was adopted in the sample preparation for the undrained tests.

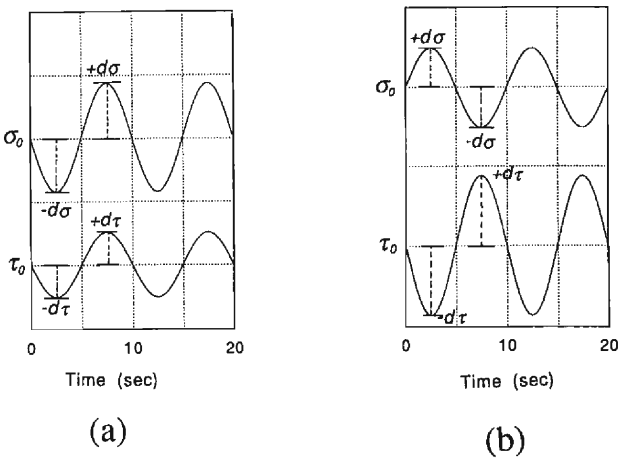

Fig. 9 Test programs of cyclic loading.
(a) : type A (vertical seismic force),
(b) : type B (horizontal seismic force).

For pumice and loess saturation, the samples were mixed with de-aired water and stirred for a few hours and left for three days for dispersion of soil aggregates. They were then stirred again to obtain a slurry sample. The sample containers were heated to about 90 C° and were shaken to release the entrapped air bubbles inside the pores. The resulting slurries were stirred for about one hour until a liquid state resulted. Before pouring the slurry into the sample box, the water path on the base of the sample box was initially filled with de-aired water. The shear box was then filled with this water up to a level over the annular metal filter of the pore pressure measuring set. The slurry was poured slowly into the shear box and the water was displaced by slurry. Samples were then left for about one day for settlement. For standard sand saturation (Toyoura sand), a dried sample was set in the sample box, and the sample box completely assembled. From the lower drainage valve, CO_2 gas was then passed through the sample. Next, de-aired water with a pressure of 0.5 kgf/cm^2 was supplied into the sample from the lower drain valve until it came out from the upper drain valve.

(3) Loading procedure : After sample setting, consolidation under normal stress of about 1.0 kgf/cm^2 was allowed to proceed, and then the samples were loaded to the initial normal stress of the tests (about 2.0 kgf/cm^2), with drainage being allowed from each end of the sample during consolidation.

To study pore pressure generation, high values of B_D(>0.95) were desirable. According to the preliminary tests, B_D value was high for the loess sample. However, in the case of pumice and the Toyoura sand, B_D values measured after consolidation were not satisfactory (<0.90). Therefore, back pressure of about 1 kgf/cm^2 and 0.7 kgf/cm^2 were used for the pumice and the Toyoura sand, respectively. Back pressure decreases the effect of any remaining air inside the sample and causes a higher value of B_D during the tests, and also results in the complete dissolution of used CO_2 gas in the water. After consolidation, the total normal stress and the back pressure were increased simultaneously by keeping the effective normal stress at 2.0 kgf/cm^2.

After checking that the B_D value was higher than 0.95 (**Table 1**), the samples were loaded to the initial shear stress using the torque control servo motor (Q in **Fig. 4**). This stage was done carefully and very slowly to avoid any accidental large shear displacement. Then the cyclic loading tests were performed.

4. Test results

Test results are presented in **Fig. 10** to **21**. Both stress changes in the total stress and in the effective stress were drawn. The loaded shear stress corresponds to the sum of the static and the seismic stress, and is not always the same as the shear resistance because the acceleration of the landslide mass consumes a portion of the loaded stress. To simulate seismic stress, the loaded shear stress was controlled by a servo motor using the value monitored by the torque transducer (C7) as feedback signal (**Fig. A–1 b**) in Appendix). The shear resistance mobilized on the shear surface during the tests was monitored by a shear load cell (C3 in **Fig. 4**). The mass of the lower half of the rotating shear box was not great and the difference between the loaded shear stress and the shear resistance was not appreciable. The loaded shear stress dropped with a drop in shear resistance after failure because of the speed limitation of the servo motor. The shear stress monitored by the torque transducer (C7) was used for the total stress path plot and the shear resistance monitored by the load cell (C3) was used for the effective stress path plot.

4. 1 Ontake pumice

(1) Loading type A : The stress paths of this test are shown in **Figs. 10 a)** and **b)**. The stress path of the total stress is a series of closed loops surrounding the previous loop. Unlike the pattern of the total stress, the effective stress path is a series of loops that move gradually leftwards due to a small amount of generated residual pore pressure. The effective dynamic friction angle (ϕ'_d) was calculated to be 38.7°. The time series data of shear displacement, pore pressure (measured at the shear zone) and cyclically loaded stresses are shown in **Fig. 11 a)**, **b)** and **c)**, respectively. At the seventh cycle, shear with the maximum velocity initiated (the maximum shear velocity was 30 cm/s, which was limited by the maximum capacity of the servo motor, (Q in **Fig. 4**).

(2) Loading type B : The total stress path, the effective stress path and the time series data of monitored values are presented in **Fig. 12** and **13**. Pore pressure build–up was not appreciable before failure, but increased sharply with the initiation of failure. Accordingly, the shear resistance decreased to a very low value. At the seventh cycle, shearing with the maximum velocity initiated. The effective dynamic friction angle (ϕ'_d) was calculated to be 38.9°, almost the same as that in the loading type A.

4. 2 Lishan Loess

(1) Loading type A : The total stress path diagram of this test is shown in **Fig. 14 a)** which shows a series of closed loops overlapping each other. The effective stress path diagram is shown in **Fig. 14 b)**. From an initial stress state (point (I)), each successive loading cycle

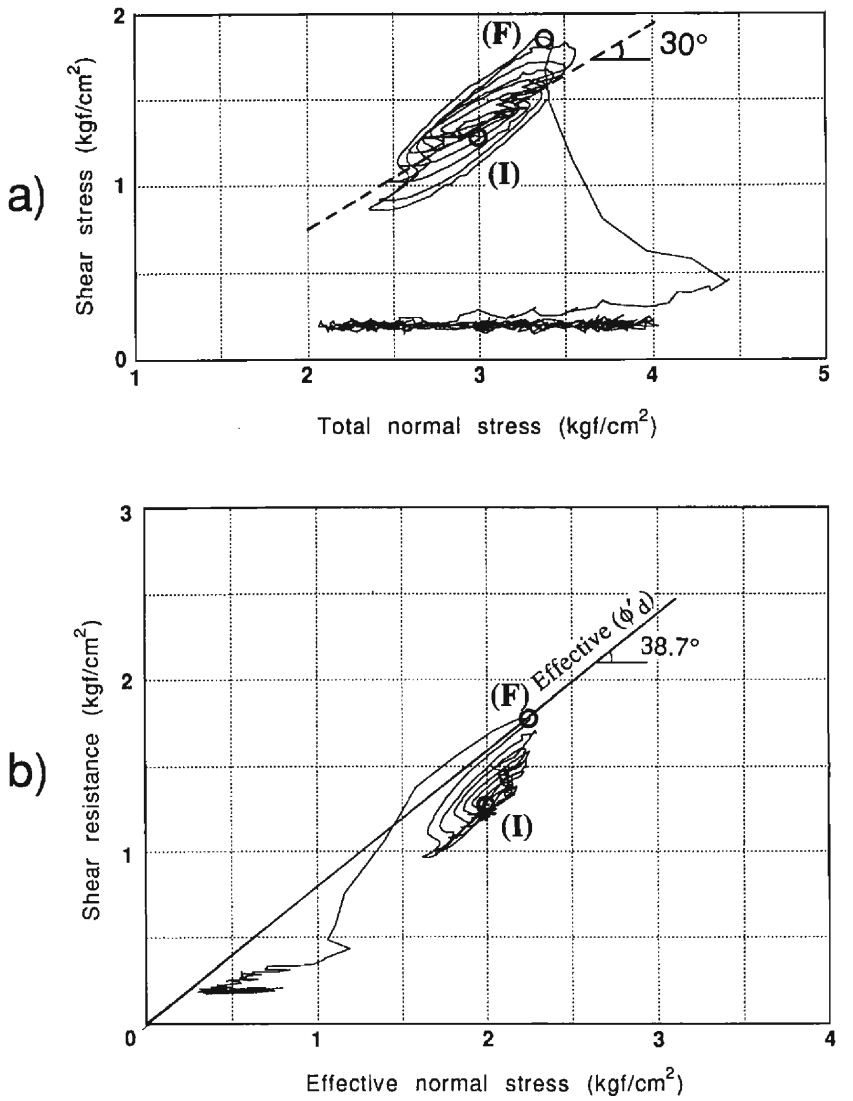

Fig. 10 Total stress path a) and effective stress path b) in the test of pumice sample (loading type A, Test Pumice–1).
(I) : initial stress point, (F) : stress point at failure, γ_d=0.70gf/cm^3, e=2.81, u_b=0.96 kgf/cm^2, B_D=0.98.

led to an increasingly positive pore pressure. This accumulation of positive pore pressure reduced the effective normal stress. The stress path moved left towards the failure line and intersected it at point (F), at which point, the shear started. Shear displacement, pore pressure (measured at the shear zone) and cyclically loaded stresses versus time plots are shown in **Fig. 15 a), b)** and **c)**, respectively. Pore pressure building–up is clearly visualized. The effective dynamic friction angle (ϕ'_d) was calculated to be 26.5°.

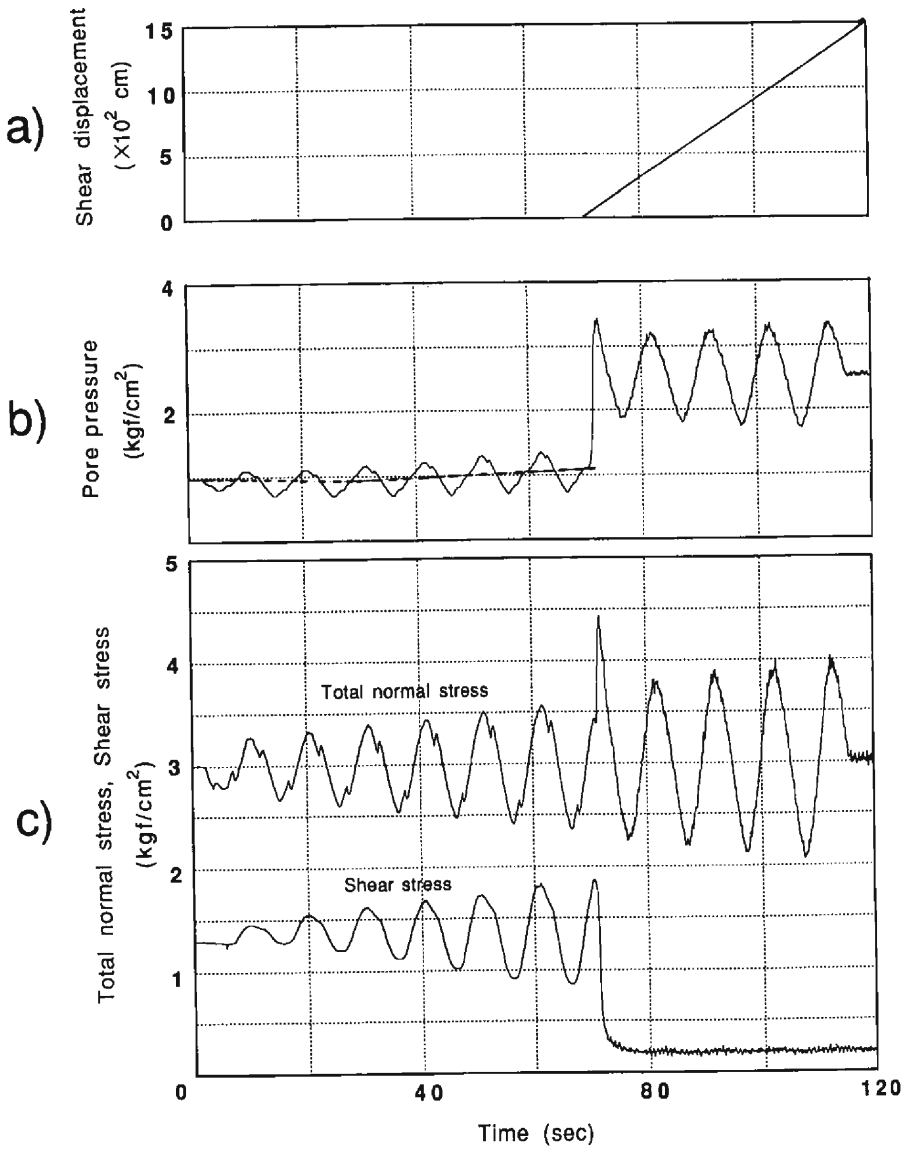

Fig. 11 Time series data of the shear displacement a), the pore pressure b) and the cyclically loaded stresses c) in the test of pumice sample (loading type A, Test Pumice–1).

(2) **Loading type B** : As with loading type A, constant amplitudes of cyclic normal stress and cyclic shear stress were applied. The total stress path and the effective stress path of this test are shown in **Figs. 16 a)** and **b)**, respectively. The effective dynamic friction angle (ϕ'_d) was calculated to be 29.8°, a little higher than that in loading type A. The time series data of Shear displacement, pore pressure and cyclically loaded stresses are shown in **Figs. 17 a), b)**

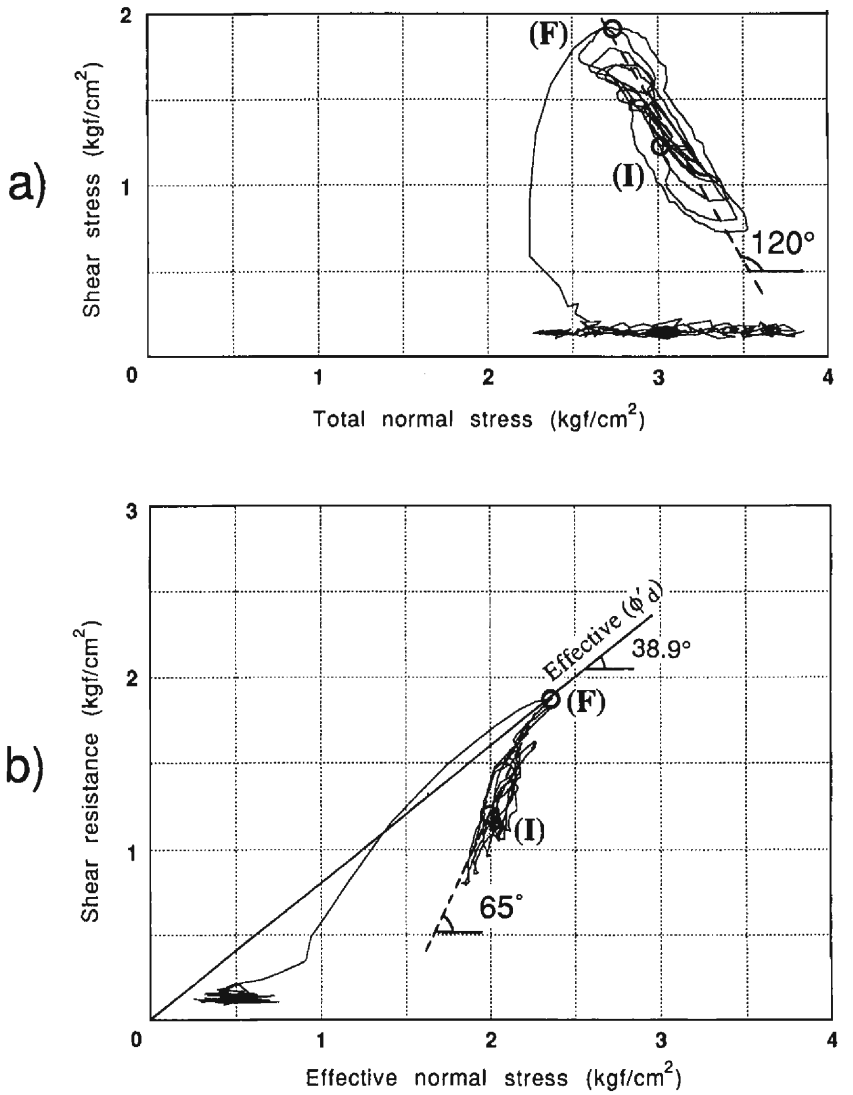

Fig. 12 Total stress path a) and effective stress path b) in the test of pumice sample (loading type B, Test Pumice-2).
(I) : initial stress point, (F) : stress point at failure, γ_d=0.71gf/cm^3, e=2.76, u_b=1.0 kgf/cm^2, B_D=0.96.

and c), respectively. No appreciable shear displacement was observed during the first 4 cycles, but at the fifth cycle, failure occurred.

4. 3 Toyoura standard sand

(1) Loading type A : The stress path of the total stress is shown in **Fig. 18 a)**, that is a

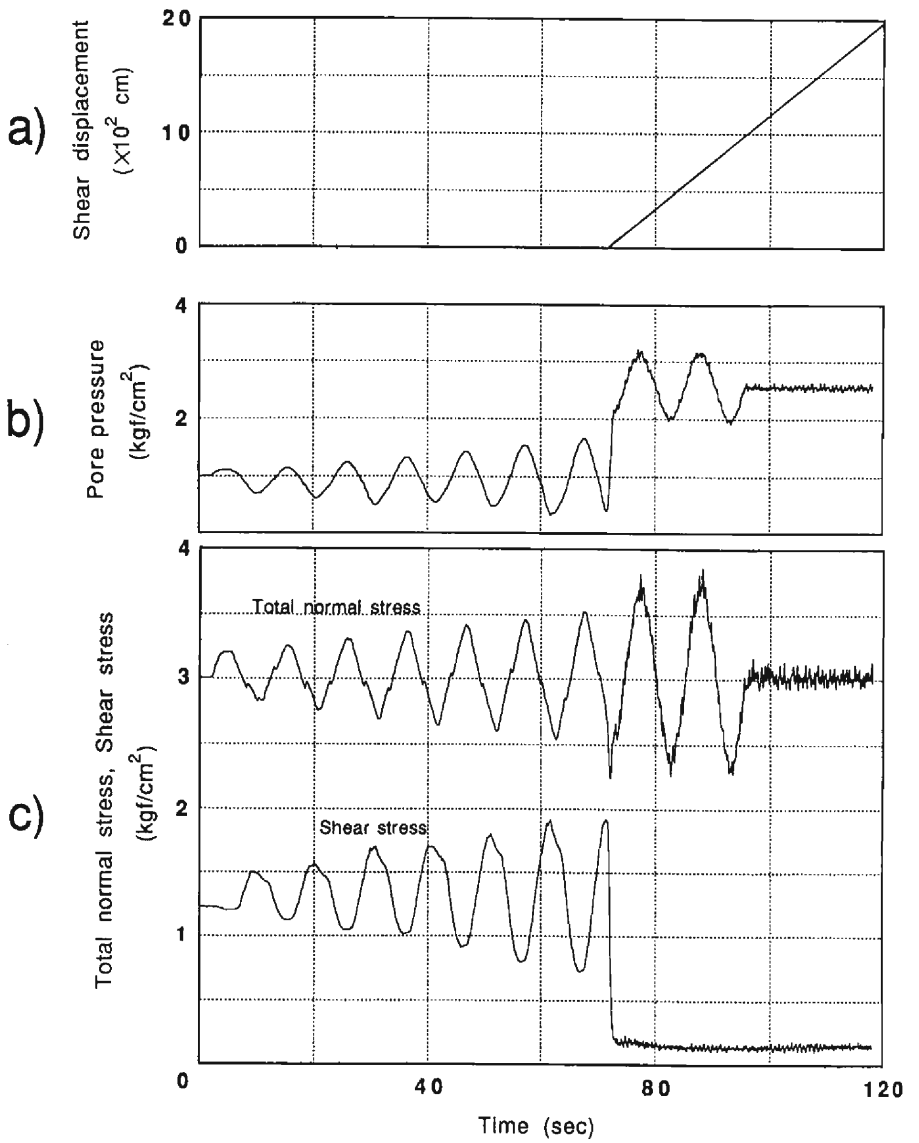

Fig. 13 Time series data of the shear displacement a), the pore pressure b) and the cyclically loaded stresses c) in the test of pumice sample (loading type B, Test Pumice-2).

series of closed loops surrounding the previous loop. Unlike the loess sample, the effective stress path (**Fig. 18 b)**) is a series of closed loops, the same as the total loaded stress without leftward shifting. Shear displacement, pore pressure and cyclically loaded stresses versus time plots are shown in **Fig. 19 a), b)** and **c)**, respectively. Only small shear displacement was observed during each cycle when the loaded stress reached the failure line. At the eighth cycle,

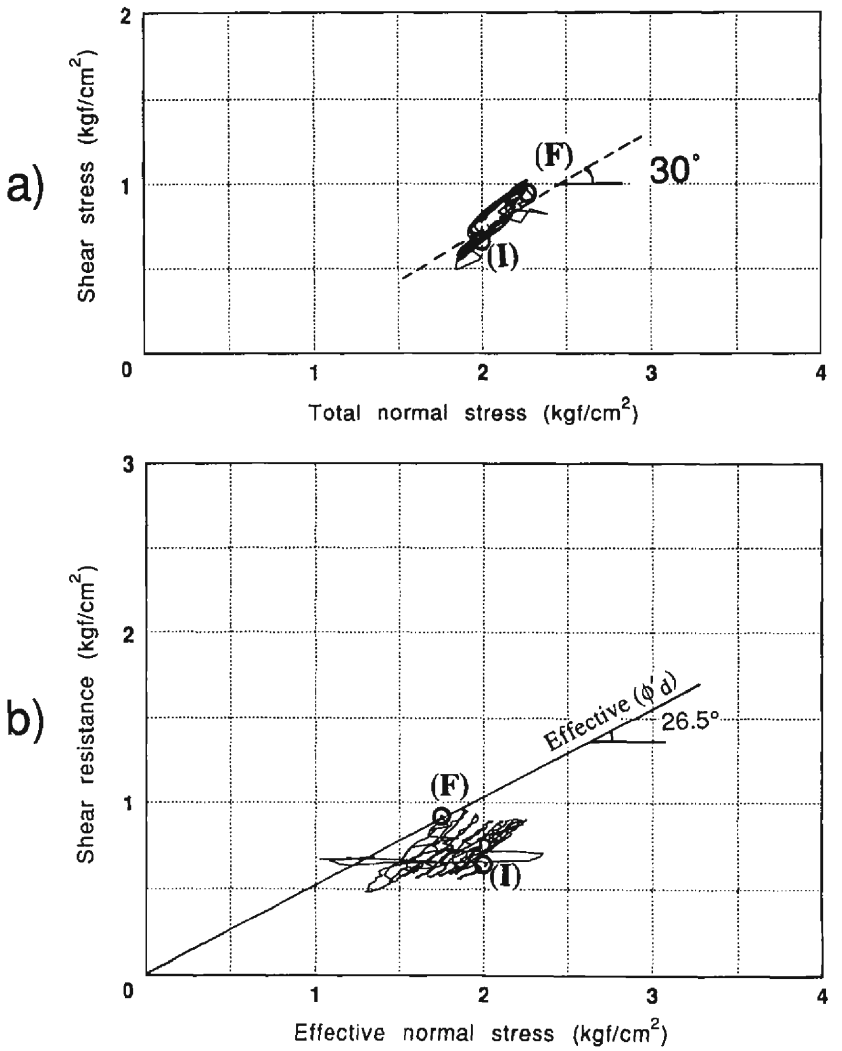

Fig. 14 Total stress path a) and effective stress path b) in the test of loess sample (loading type A, Test Loess-1).
(I) : initial stress point, (F) : stress point at failure, γ_d=1.58gf/cm³, e=0.79, u_b=0, B_D=0.98.

the effective dynamic friction angle (ϕ'_d) was calculated to be 35.0°.

(2) Loading type B : As shown in **Fig. 20 a)**, the total stress in the stress diagram is nearly a straight line. Unlike the linear total stress path, the effective stress path (**Fig. 20 b)**) is a series of closed loops surrounding the previous loop. Shear displacement, pore pressure and cyclically loaded stresses versus time plots of this test are shown in **Fig. 21 a), b)** and **c)**, respectively. Only small shear displacement was observed after failure. The effective dynamic

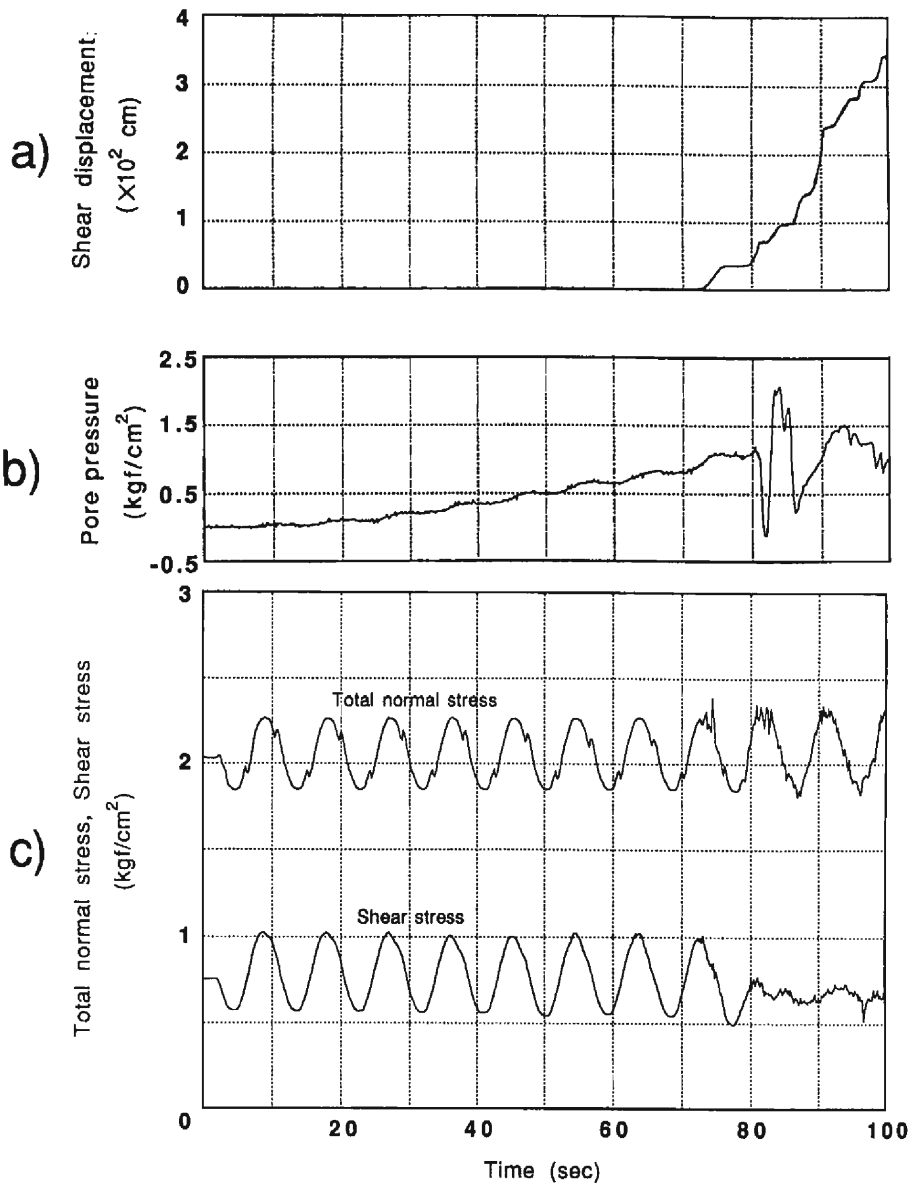

Fig. 15 Time series data of the shear displacement a), the pore pressure b) and the cyclically loaded stresses c) in the test of loess sample (loading type A, Test Loess–1).

friction angle (ϕ'_d) was calculated to be 36.8°, a little higher than that in loading type A.

4.4 General remarks

The results of the pumice sample showed that it has almost the same strength for both

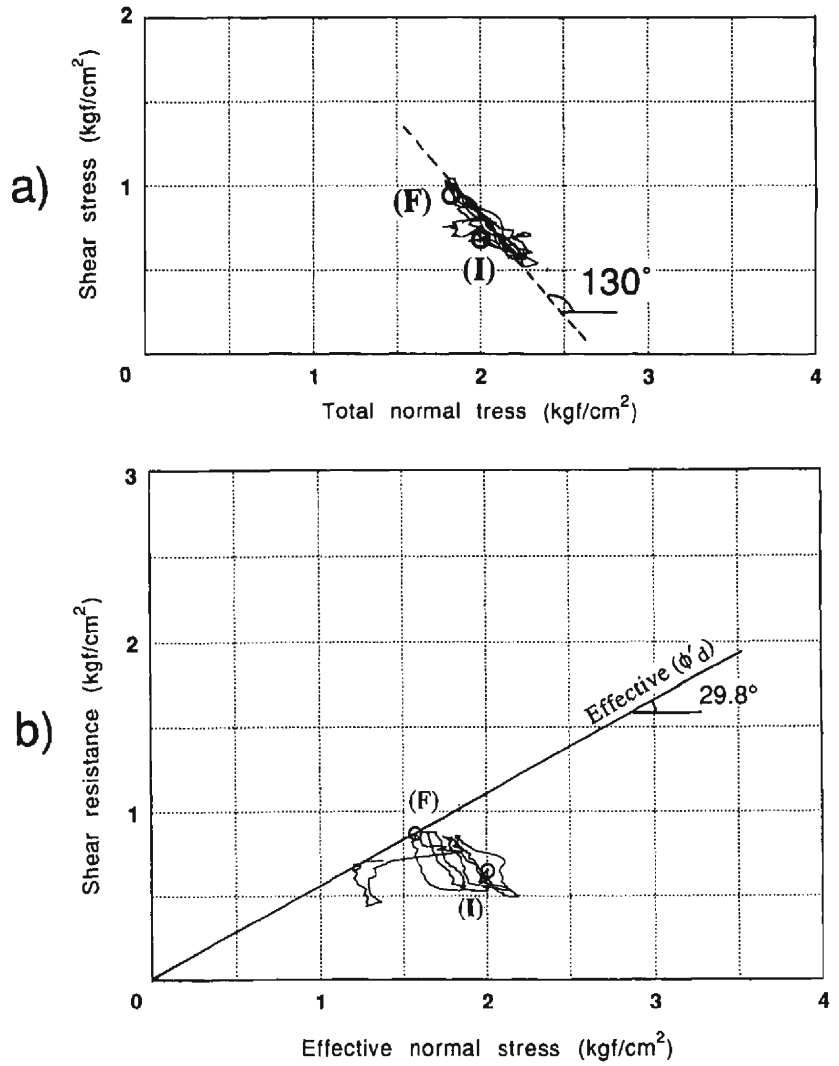

Fig. 16 Total stress path a) and effective stress path b) in the test of loess sample (loading type B, Test Loess-2).
(I) : initial stress point, (F) : stress point at failure, $\gamma_d = 1.59 gf/cm^3$, $e = 0.79$, $u_b = 0$, $B_D = 0.97$.

types of cyclic loading. Before failure, the generation of positive and negative pore pressure was proportional to the cyclically loaded stresses, but the positive pore pressure increased sharply due to the collapse of the soil skeleton after failure. In the undrained shearing, collapse of the structure results in the load being suddenly transferred from the grain skeleton to the pore water, causing a sharp increase in pore water pressure. As a result, the shear strength

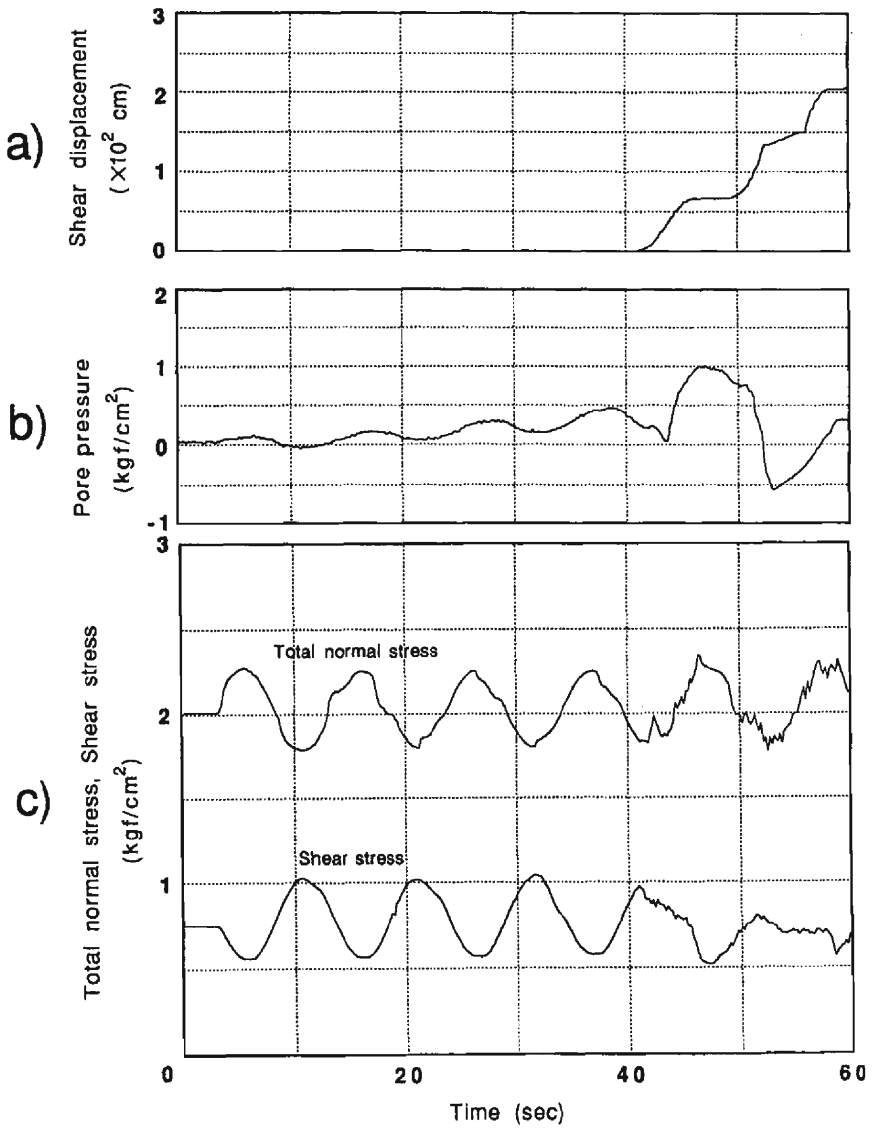

Fig. 17 Time series data of the shear displacement a), the pore pressure b) and the cyclically loaded stresses c) in the test of loess sample (loading type B, Test Loess-2).

is substantially reduced, and the sample undergoes a rapid deformation. In both tests for different types of cyclic loading, after failure the loaded shear stress showed a sudden drop and remained at a minimum value of about 0.2 kgf/cm^2 (much smaller than the initial loaded shear stress). It can be concluded that, slopes composed of pumice have relatively high shear strengths (38.7°～38.9° in the dynamic friction angle) during earthquakes. However, when

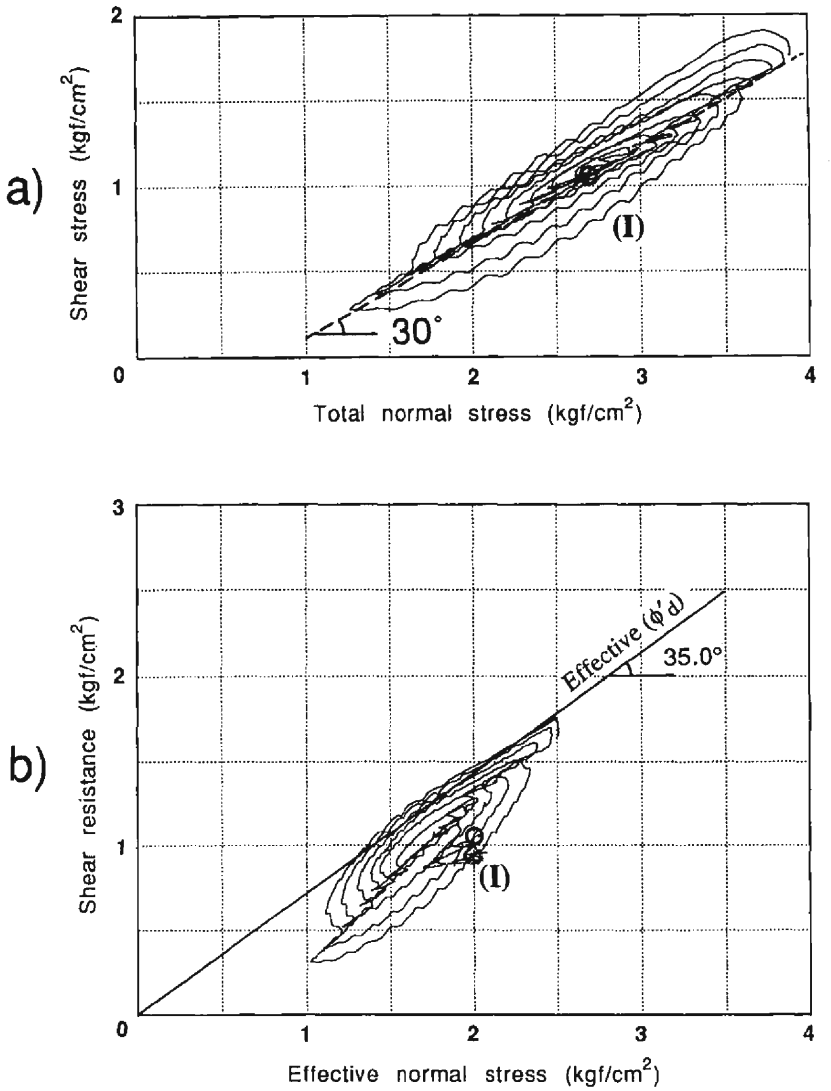

Fig. 18 Total stress path a) and effective stress path b) in the test of Toyoura sand sample (loading type A, Test T–Sand–1).
(I) : initial stress point, $\gamma_d = 1.48 gf/cm^3$, $e = 0.78$, $u_b = 0.73 kgf/cm^2$, $B_D = 0.97$.

the seismic stress reaches the failure line, rapid failure occurs with a long travel distance.

In the case of the loess sample, pore pressure built up gradually during cyclic loading before failure. After shear started, unlike the pumice sample, no sudden increase in pore pressure and no drop in the loaded shear stress was observed. Shear velocity was low, a series of start–stop shearing was found during each cycle. It can be concluded that landslides in slopes

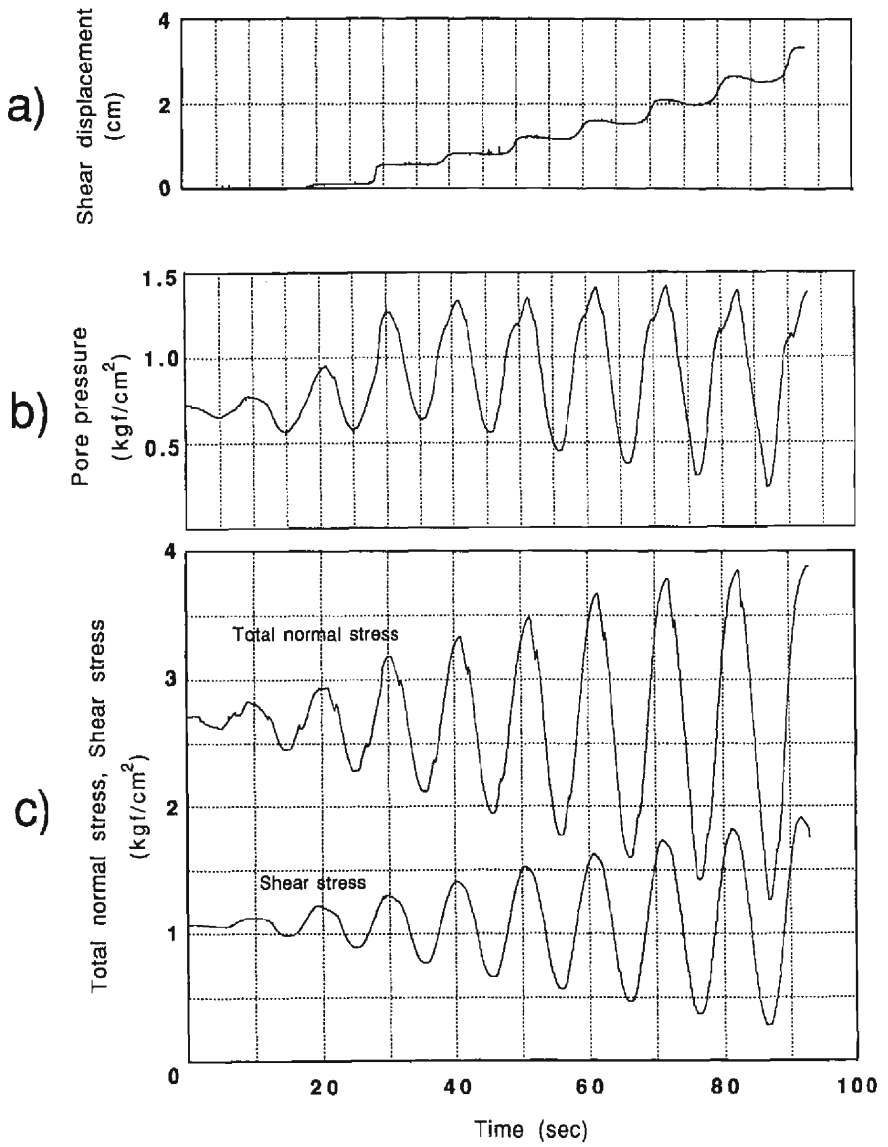

Fig. 19 Time series data of the shear displacement a), the pore pressure b) and the cyclically loaded stresses c) in the test of Toyoura sand sample (loading type A, Test T–Sand–1).

that are composed of loess can be triggered by relatively small amplitude of earthquake loading, but it will not be a rapid failure.

In the case of Toyoura standard sand, the well–rounded and well–sorted grains of sands resulted in a non–collapsible texture. Small strain along the shear zone did not result in generation of pore pressure. In the loading type A and B tests, only small shear displacement was

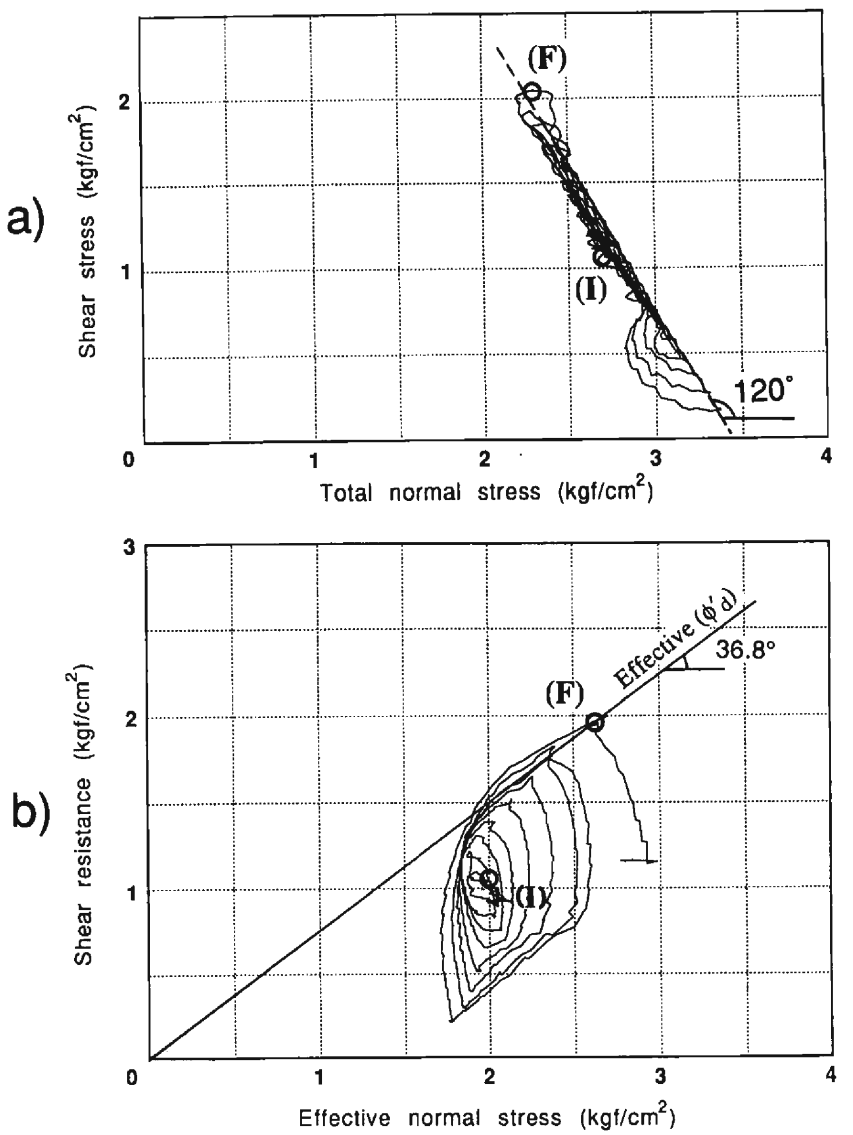

Fig. 20 Total stress path a) and effective stress path b) in the test of Toyoura sand sample (loading type B, Test T–Sand–2).
(I) : initial stress point, (F) : stress point at failure, $\gamma_d = 1.48 gf/cm^3$, $e = 0.78$, $u_b = 0.70$ kgf/cm², $B_D = 0.98$.

observed when the loaded shear stress reached the failure line during each cycle. In this case, even if failure initiated (test T–Sand–2 in **Fig. 21 a**)) the shear velocity would be very low with a small, limited shear displacement. No sudden decrease in loaded shear stress was observed.

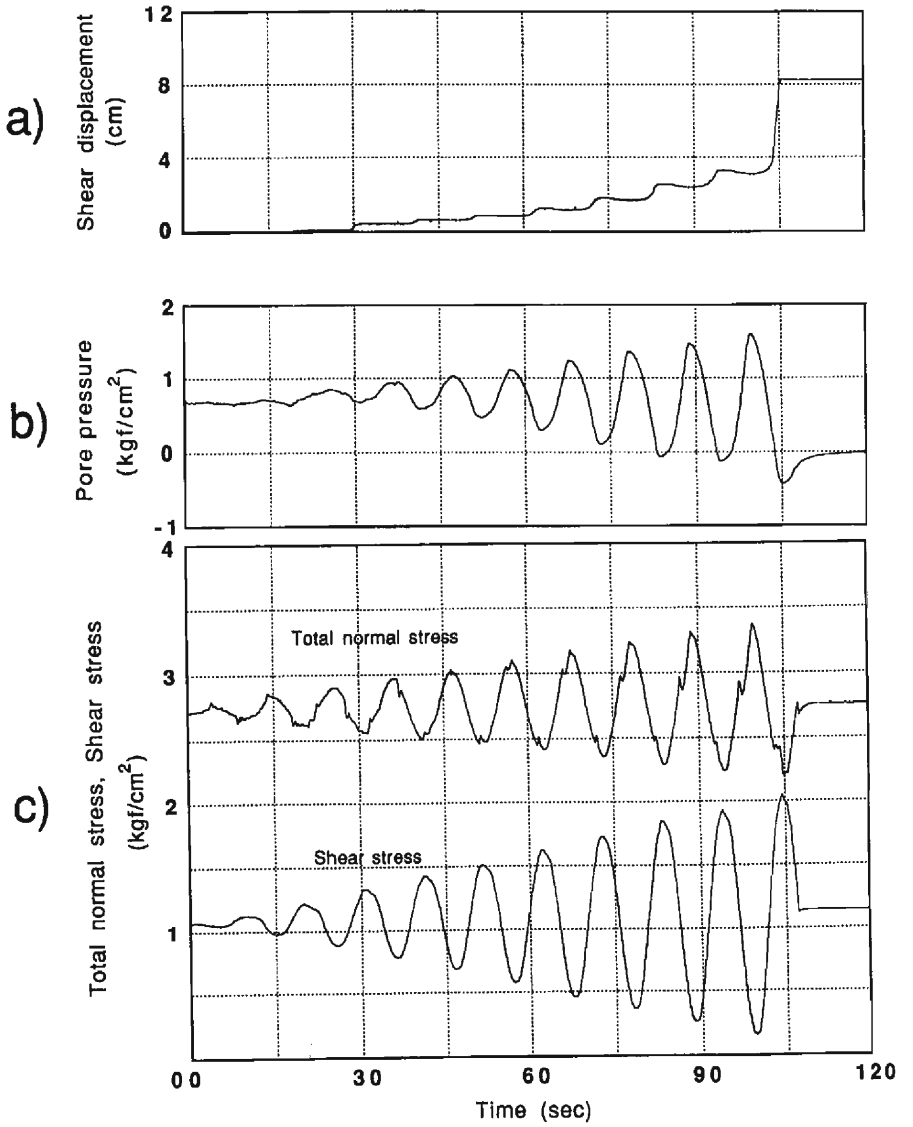

Fig. 21 Time series data of the shear displacement a), the pore pressure b) and the cyclically loaded stresses c) in the test of Toyoura sand sample (loading type B, Test T–Sand–2).

5. Discussion of the test results

5.1 Pore pressure parameters and effective stress direction

When a saturated soil deposit is subjected to cyclic loading in both normal stress and the shear stress directions, pore pressure will change depending on the state of the soil (dilative or compressible). Such change in the pore pressure is the most important component of the

cyclic characterization of soil deposits. Generation of pore pressure due to the stress increment can be expressed as Skempton [14] did in the undrained triaxial compression test :

$$\Delta u = B(\Delta\sigma_3 + A(\Delta\sigma_1 - \Delta\sigma_3)) \tag{5-1}$$

where A and B : pore pressure parameters, $\Delta\sigma_1$, $\Delta\sigma_3$: increment of principal stresses.

Analogous to this equation, Sassa *et al.* [15] and Sassa [16] suggested that pore pressure generation under the undrained direct shear state can be expressed as follows :

$$\Delta u = B_D(\Delta\sigma + A_D\Delta\tau) \tag{5-2}$$

where $\Delta\sigma$, $\Delta\tau$: increment of normal and shear stresses, A_D, B_D : Pore pressure parameters in the direct shear state.

For fully saturated soil $B_D=1.0$, the effective normal stress in the undrained ring shear test (that is the direct shear state) is presented from Equation (5-2) :

$$\Delta\sigma' = \Delta\sigma - \Delta u = -A_D\Delta\tau \tag{5-3}$$

When the soil along the shear zone is in a dilative state, A_D value is negative and the effective normal stress increases ($+\Delta\sigma'$) with increments of the shear stress ($+A\tau$). When the soil along the shear zone is in a compressible state, A_D value is positive and the effective normal stress decrease ($-\Delta\sigma'$) with increments of shear stress ($+\Delta\tau$). For soil of $A_D=0$ the increment of the effective normal stress is zero.

For all the tests of this study, the B_D values after completion of consolidation were found to be between 0.96 to 0.98. Considering $B_D=1.0$, the value of A_D can be calculated as follows :

$$\Delta u = \Delta\sigma + A_D\Delta\tau \tag{5-4}$$

$$A_D = -\frac{(\Delta\sigma - \Delta u)}{\Delta\tau} \tag{5-5}$$

Using Equation (5-5) the value of A_D was calculated from $\Delta\sigma(n)$, $\Delta\tau(n)$ and $\Delta u(n)$ for n_{th} cycles until just before the failure started (n : number of cycles) as shown in **Fig. 22**. Plots of the calculated A_D values versus the number of cycles of type A and B loading tests are shown in **Figs. 23 a)** and **b)**, respectively.

In type A loading (**Fig. 23 a)**), A_D values in all samples were negative and almost all of values were within the range of -0.8 to -1.4. In type B loading (**Fig. 23 b)**), A_D values in these samples were quite different. A_D values were negative in pumice, positive in loess and changed from the positive to negative in Toyoura sand.

A negative A_D value means that the effective stress path has an up-right direction in the stress diagram, it is similar to the total stress direction in the vertical seismic loading. A positive A_D value means an up-left effective stress direction, and is similar to the loaded stress

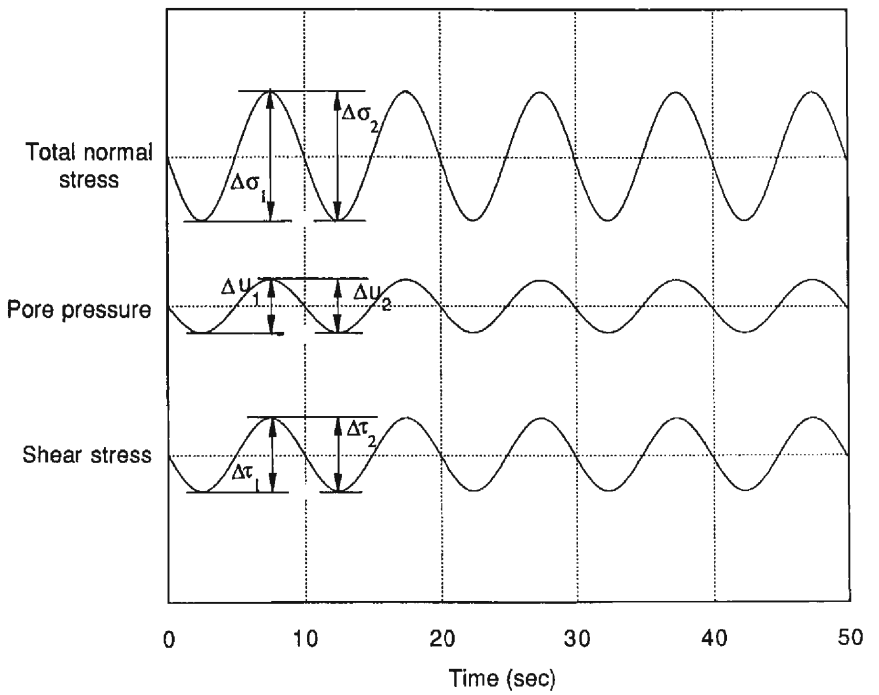

Fig. 22 Calculation of A_D value from the test results.

direction in the case of horizontal seismic loading.

(1) Stress direction in the tests of loading type A: In the case of pumice sample (loading type A, **Fig. 10 a)**), the direction of the cyclically loaded total stress on the stress diagram was around 30°. The effective stress path diagram of this test is shown in **Fig. 10 b)**. The direction was almost similar, but showed a slight shift to the left. The movement of the open loops of the effective stress path toward the failure line is due to a small increase of the residual pore pressure (**Fig. 11 b)**).

In the case of loess sample (loading type A, **Fig. 14 a), b)**), the direction of the total stress path on the stress diagram is around 30°. The effective stress path of this test was almost similar to that of the loaded total stress, but loops of the effective stress path shift gradually to the left towards the failure line.

In the Toyoura sand test, **Fig. 18 a)** and **b)**, the direction of the total stress on the stress diagram is around 30° and the effective stress path has a similar up–right direction.

(2) Stress direction in the tests of loading type B: In pumice sample (**Fig. 12 a)**) the cyclically loaded total stress path on the stress diagram has an angle around 120°. However, the effective stress path (**Fig. 12 b)**) has an angle of about 65° and is quite different from that of the total stress.

In the case of the loess sample (**Fig. 16 a)**) in which, the direction of the total stress path in the stress diagram is around 130°, no great difference between the total stress direction (**Fig.**

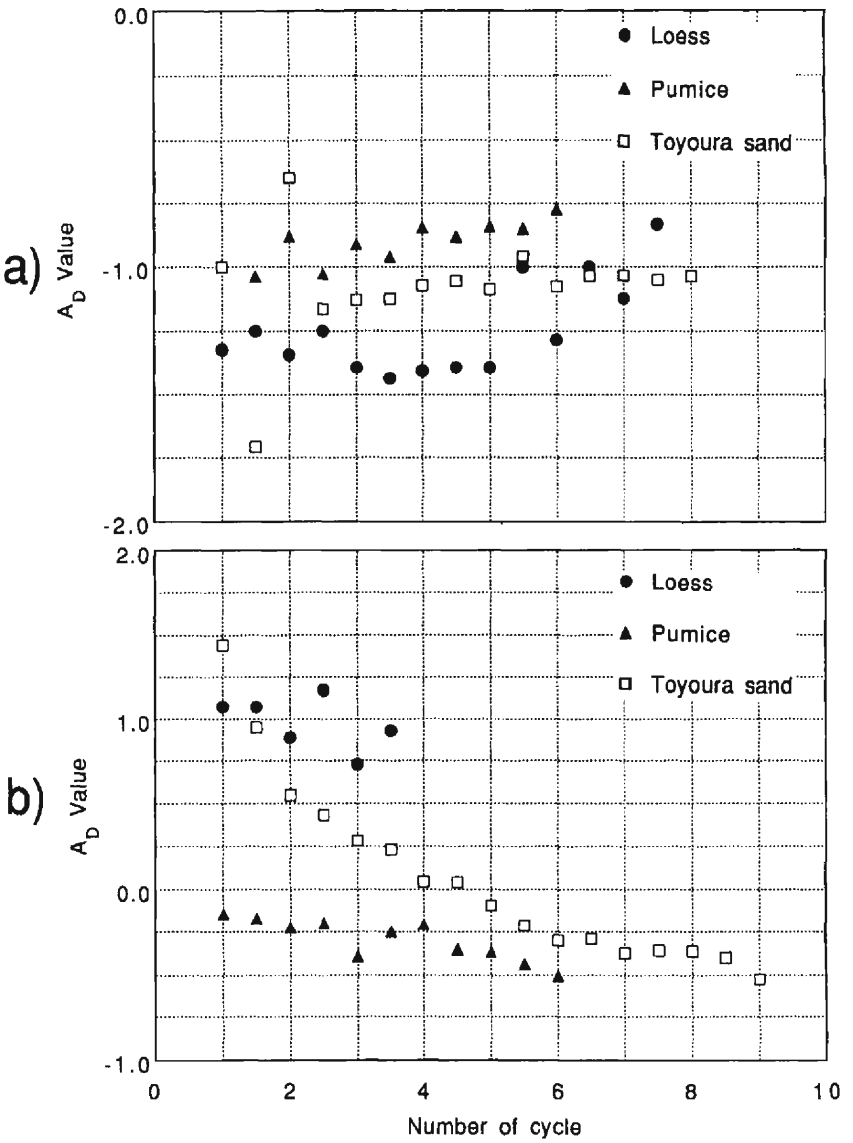

Fig. 23 A_D values of the tests of loading type A a), and loading type B b).

16 b)) and effective stress direction was observed.

In the Toyoura sand test (test T–Sand–2), unlike the direction of the cyclically loaded total stress that has an angle around 120° (**Fig. 20 a**)), the effective stress path has different angles during each cycle (**Fig. 20 b**)). It is vertical in some parts (A_D value is almost zero). However, its direction approaches that of the failure line in its upper part (negative A_D value).

The loops of the effective stress path of Toyoura sand are wider than those of pumice due to a different mechanism of pore pressure generation during each cycle.

In fully saturated soils in which the B_D value is unity, soil behavior is controlled by the A_D value, which varies according to sample and loading types. Though the difference of A_D values in vertical loading (type A) was not great, it was rather diverse in the horizontal loading (type B) (see **Fig. 23 a**) and **b**)).

The effective stress path direction is a very important factor in controlling the magnitude of seismic loading necessary to cause failure.

5. 2 Application

In the cyclic loading test procedure, first, the sample is subjected to an initial normal stress (σ_0) and an initial shear stress (τ_0) corresponding to the given potential sliding surface in the field (**Fig. 24 a**)). The initial shear stress in the field can be defined as :

$$\tau_0 = W \cdot \sin\theta \qquad (5\text{–}6)$$

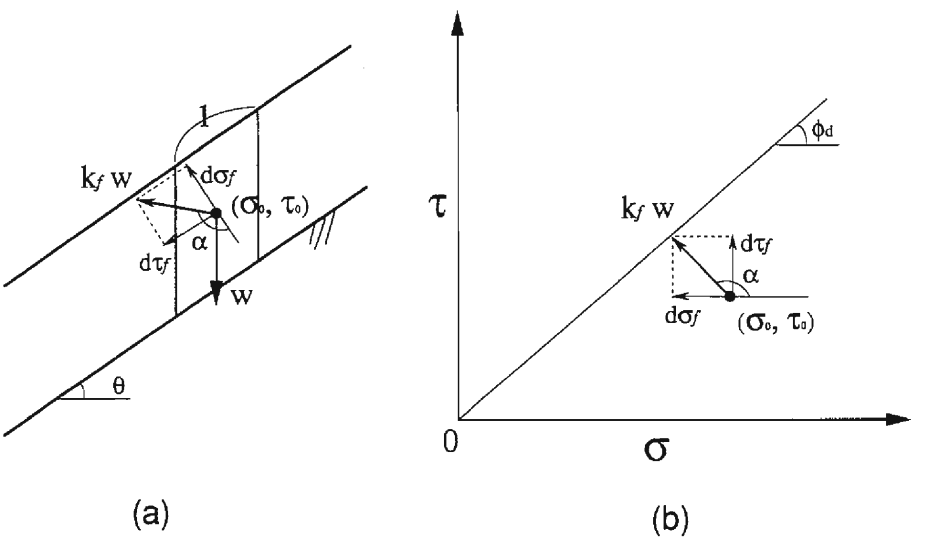

σ_0, τ_0 : Initial stress , W: Total weight of the soil column having a unit length along the slope, k_f W: Seismic stress necessary to cause failure, $d\tau_f$: Increment of shear stress on the shear plane (shear resistance) at failure, $d\sigma_f$: Increment of normal stress on the shear plane at failure, ϕ_d: Dynamic friction angle, θ: Slope angle, α: Angle between the direction of the seismic stress and the normal stress to the sliding surface.

Fig. 24 Illustration of the earthquake loading in the slope (a) and in the stress diagram (b).

where τ_0: initial shear stress, θ: slope angle in consideration, W: total weight of the soil column having a unit length along the slope.

Using the initial stress and the failure line of the dynamic friction angle (**Fig. 24 b**)), the seismic coefficient necessary to cause failure (k_f) acting on a column in the slope is expressed as follows[9), 10)];

$$k_f W = \sqrt{d\sigma_f^2 + d\tau_f^2} \tag{5-7}$$

where ($d\tau_f$) and ($d\sigma_f$) are increments of shear and normal stresses at failure.

From equation (5–6) and (5–7),

$$k_f = \frac{\sqrt{d\sigma_f^2 + d\tau_f^2}}{\tau_0} \cdot \sin\theta \tag{5-8}$$

For each sample, almost the same initial stress levels of the normal stress and the shear stress were loaded, followed by cyclic loading tests of two different types. Using the Equation (5–8), the seismic coefficient (k_f) which is necessary to cause failure can be estimated from; 1) slope angle (θ), (30° was used for all tests), 2) initial shear stress (τ_0) and 3) the increments of the shear stress ($d\tau_f$) and the normal stress ($d\sigma_f$) at failure obtained from the test results. A summary of the cyclic loading test conditions and the calculated seismic coefficients are listed in **Table 2**.

Seismic loading may strike the slopes from various directions, horizontal loading is considered to be much more dangerous than vertical loading during an earthquake. Therefore, horizontal seismic force is usually considered in slope stability analysis (Ohne and Narita[17)], Graham[18)]). To discuss the effect of the stress direction on soil strength, three ideal cases are illustrated in **Fig. 25**. AB and AC are the directions in which the seismic stress is horizontal and parallel to the sliding surface, respectively. The seismic stress necessary to cause failure in the AC direction is greater than in AB, and no failure is expected if the seismic stress is vertical (AD direction). This hypothesis may be true for dry or partially saturated soils that generate no pore water pressure. However, in the case of saturated soils, the strength of the soil is highly affected by the direction of the effective stress that is controlled by pore pressure generation.

The tests results of the pumice and loess samples showed that the seismic coefficient necessary to cause failure for two different directions of the cyclically loaded total stress showed no appreciable difference for each sample, though a slight difference was observed in the Toyoura sand results (k_{fu}, **Table 2**). **Fig. 26 a**) and **b**) present initial stress (point A (σ_0, τ_0)), the stress increments of the shear stress ($d\tau_f$) and the total normal stress ($d\sigma_f$) at failure in the test of pumice (Test Pumice–2) and of Toyoura sand (Test T–Sand–2) respectively. In test Pumice–2 (**Fig. 26 a**)) in which the seismic stress is horizontal, if no pore pressure was generated (i. e., dry sample or in the test under drained condition), the cyclic loading with the amplitude of AB would be enough to cause failure and the calculated seismic coefficient (k_{fd}) of this direction would be 0.13. However, the test result clarified the fact that the effective stress direction (up–right) was different from the loaded seismic stress direction (up–left)

Table 2 Cyclic loading conditions and the results of the tests.

Sample, (test No.)	τ_0 kgf/cm^2	σ_0 kgf/cm^2	τ_f kgf/cm^2	$\sigma_{f\,(\mathrm{total})}$ kgf/cm^2	$d\tau_f$ kgf/cm^2	$d\sigma_f$ kgf/cm^2	$\tan^{-1}t_f/\sigma_{f\,(\mathrm{eff})}$ ϕ'_d	u_b : kgf/cm^2	k_{fu}	k_{fd}	k_{fu}/k_{fd}
Pumice (Pumice–1)	1.24	2.02	1.81	2.41	0.57	0.39	38.7°	0.96	0.28	no failure	—
Pumice (Pumice–2)	1.23	2.00	1.91	1.81	0.68	0.20	38.9°	1.0	0.29	0.13	2.23
Loess (Loess–1)	0.7	2.04	0.94	2.27	0.24	0.23	26.5°	0	0.24	no failure	—
Loess (Loess–2)	0.7	2.01	0.92	1.78	0.22	0.23	29.8°	0	0.23	0.28	0.82
Toyoura sand (T–Sand–1)	1.07	1.96	1.99	3.01	0.84	1.02	35.0°	0.73	0.62	no failure	—
Toyoura sand (T–Sand–2)	1.07	2.01	2.05	1.58	0.98	0.43	36.8°	0.70	0.50	0.17	2.94

τ_0, σ_0: Initial shear stress and initial normal stress before cyclic tests, τ_f, σ_f: Shear stress and normal stress at failure, $d\tau_f$, $d\sigma_f$: Increment of shear stress and normal stress at failure ϕ'_d: Effective dynamic friction angle, u_b: Back–pressure, k_{fu}: Seismic coefficient to cause failure under undrained state which is obtained from the test results, k_{fd}: Seismic coefficient causing failure under drained state which is estimated from the initial stress (σ_0, τ_0) and the dynamic friction angle (ϕ'_d), k_{fu}/k_{fd}: Seismic coefficient ratio.

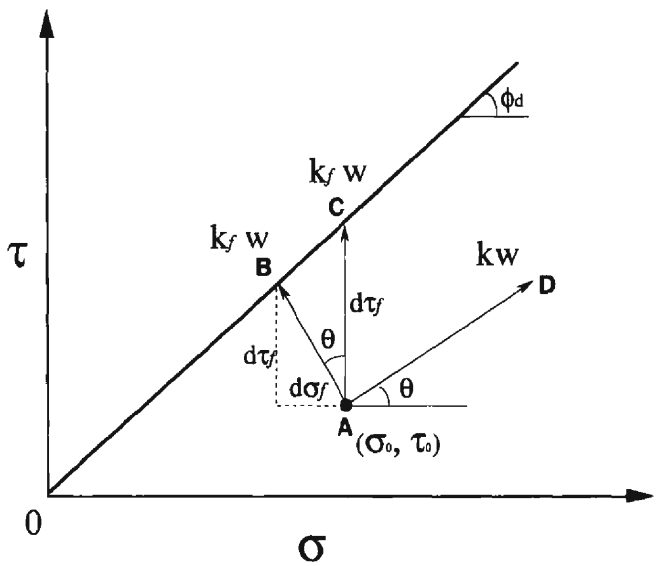

σ_0, τ_0: Initial stress , kW: Seismic stress, k_f W: Seismic stress necessary to cause failure, $d\tau_f$: Increment of shear stress on the shear plane at failure, $d\sigma_f$: Increment of normal stress on the shear plane at failure, ϕ_d : Dynamic friction angle, θ: Slope angle

Fig. 25 Illustration of three possible seismic stress directions in the stress diagram when the seismic force is horizontal (AB), parallel to the sliding surface (AC) or is vertical (AD).

because pore pressure was generated. In this case, the seismic coefficient necessary to cause failure (k_{fu}) was calculated to be 0.29 and the seismic coefficient ratio (k_{fu}/k_{fd}) in this test was 2.23.

A similar conclusion can be derived for the Toyoura sand. If no change in the effective stress direction occurs, the cyclic loading amplitude necessary to intersect the failure line is AB shown in **Fig. 26 b**). The calculated seismic coefficient necessary to cause failure (k_{fd}) for AB is 0.17. But in the undrained test, the effective stress direction was up–right (in the stress diagram), and the seismic coefficient necessary to cause failure (k_{fu}) was calculated to be 0.50. The seismic coefficient ratio (k_{fu}/k_{fd}) for this test was calculated to be 2.94. Therefore, the seismic coefficient necessary to cause failure in the undrained state would be two times greater than that of the drained state.

These test results showed that, in saturated soils, it is not possible to estimate the seismic coefficient necessary to cause failure from the initial stress and the effective dynamic friction angle if no pore pressure generation is considered.

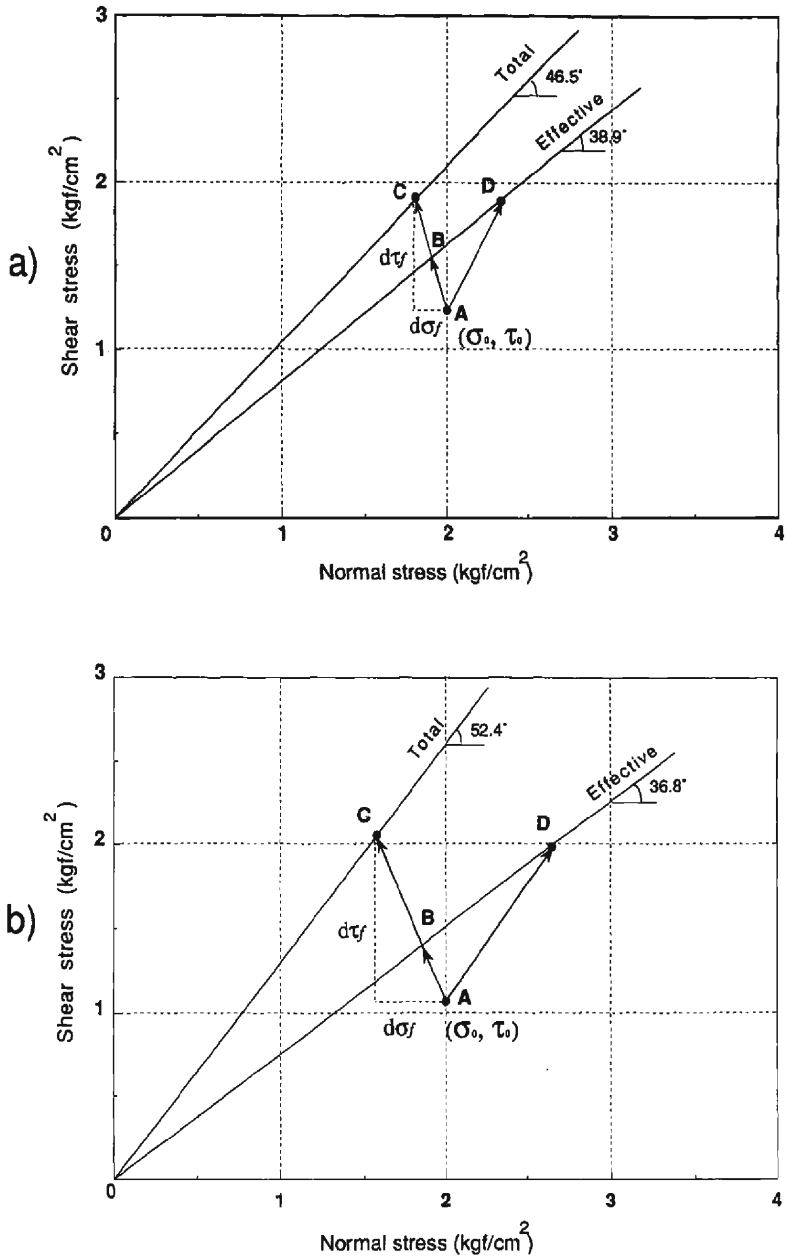

Fig. 26 Stress paths for the pumice and the Toyoura sand samples to cause failure in the test of loading type B, a) : Test Pumice-2, b) : Test T-Sand-2) ; AC : total stress increment in the undrained condition, AD : effective stress increment in the undrained condition, AB : the stress increment in the drained condition.

6. Conclusion

(1) Cyclic loading ring shear tests were carried out using a newly developed apparatus. To simulate the seismic stress loading in soil element of a slope under the undrained state, the sample box of this apparatus was improved for undrained tests and could measure pore pressure along the shear zone. This improved apparatus and the test methods adopted in this study can be used to assess the seismic stress level necessary to cause failure and also to predict the initial velocity of movement in slopes.

(2) The test results of pumice and loess suggest the following : In slopes of pumice, when the seismic stress level reaches the critical stress level, a rapid landslide should occur due to extremely great pore pressure generation. Landslides in slopes that are composed of loess can be triggered by a relatively small amplitude of earthquake loading as a result of the pore pressure build-up, but it would move with a moderate velocity.

(3) The effect of vertical and the horizontal forces of earthquakes in slopes was considered separately for tests procedures. For this purpose, two types of loading in which the cyclically loaded stress is vertical or horizontal were applied. In slope stability analysis, horizontal loading has so far been considered to be much more dangerous than vertical loading. However, this study suggests that, the respective seismic coefficients necessary to cause failure for the two types of cyclically loaded stress have no appreciable difference. This is due to the change in the effective stress direction in the undrained conditions.

(4) The difference in dynamic friction angles between these two types of loading is not great, almost the same in pumice and 2~3 degrees in loess and Toyoura sand. If the soil in a slope is in the drained condition, it is possible to predict the seismic coefficient that causes failure from the initial stress and the dynamic friction angle. However, if the soils are saturated and are in the undrained state during earthquakes, the seismic coefficient necessary to cause failure can be quite different from that in the drained condition.

Acknowledgment

This paper was submitted by Z. Shoaei for the degree of doctor of science, Kyoto University.

Research Associate Hiroshi Fukuoka and postgraduate students of the Landslide Section, Disaster Prevention Research Institute, Kyoto University are acknowledged for their cooperation throughout this work.

Thanks are due to the Associate Professor Yoshimasa Kobayashi, the Geophysical Institute of the Faculty of Science, Kyoto University for his helpful advice.

References

1) Seed, H. B. and K. L., Lee : Liquefaction of Saturated Sand During Cyclic Loading, ASCE, No. CM6, Vol. 92, 1966, pp. 105–134.

2) Seed, H. B. and W. H. Peacock : Test Procedures for Measuring Soil Liquefaction Characteristic, ASCE, No. SM8, Vol. 97, 1971, pp. 1099–1119.

3) Ishihara, K. and S. Yasuda: Sand Liquefaction in Hollow Cylinder Torsion under Irregular Excitation, Soil and Foundation, No. 1, Vol. 15, 1975, pp. 45–59.
4) Shibata, T. and H. Yukitomo: Shear Strength of Sand under a Vibrating Load, Bull. Disas. Prev. Res. Inst., Kyoto Univ., Vol. 19, Part 3, 1970, pp. 27–37.
5) Ishihara, K.: Stability of Natural Deposits During Earthquake, Proc. 11th International Conference on Soil Mechanics and Foundation Engineering, San Francisco, Vol. 1, 1985, pp. 321–376.
6) Bishop, A. W., G. E. Green, V. K. Garga, A. Andresen and J. D. Brown: A New Ring Shear Apparatus and its Application to the Measurement of Residual Strength, Géotechnique, Vol. 21(4), 1971, No. 4, pp. 273–328.
7) Lemos, L. J. L., A. W. Skempton and P. R. Vaughan: Earthquake Loading of Shear Surface in Slopes, Proc. 11th International Conference on Soil Mechanics and Foundation Engineering, San Francisco, Vol. 4, 1985, pp. 5–8.
8) Yatabe, R., N. Yagi and M. Enoki: Ring Shear Characteristics of Clays in Fractured-Zone-Landslide, Sixth International Symposium on Landslides, Christchurch, New Zealand, "Landslides", Vol. 1, Bulkema., 1992, pp. 607–612.
9) Sassa, K.: Access to the Dynamics of Landslides During Earthquakes by a New Cyclic Loading High-Speed Ring Shear Apparatus, Theme Address, Sixth International Symposium on Landslides, Christchurch, New Zealand, "Landslides", Vol. 3, Bulkema, 1993, 20 pages. (in print).
10) Shoaei, Z. and K. Sassa: Mechanism of Landslide Triggered by the 1990 Iran Earthquake, Bull. Disas. Prev. Res. Inst., Kyoto Univ., Vol. 43, Part 1, 1993, pp. 1–29.
11) Peacock, W. H. and H. B. Seed: Sand Liquefaction under Cyclic Loading Simple Shear Condition, ASCE, No. SM3, Vol. 94, 1968, pp. 689–708.
12) Brown, S. F., A. K. F. Lashine and A. F. L. Hyde: Repeated Load Triaxial Testing of a Silty Clay, Géotechnique, 25(1), 1975, pp. 95–1975.
13) Pande, G. N. and O. C. Zienkiewicz: Soil Mechanics-Transient and Cyclic Loads, Constitutive Relation and Numerical Treatment, John Wiley & Sons Ltd., 1982, 627 pages.
14) Skempton, A. W.: The Pore Pressure Coefficients A and B, Géotechnique, No. 4(4), 1954, pp. 143–147.
15) Sassa, K., M. Kaibori and N. Kitera: Liquefaction and Undrained Shear of Torrent Deposits as the Cause of Debris Flow, Proc. Inter. Symp. on Erosion, Debris flow and Disas. Prev., Tsukuba, 1985, pp. 231–236.
16) Sassa, K.: Geotechnical Model for the Motion of Landslides, Proc. 5th Inter., Symp. on Landslides, Lausanne, 1988, pp. 37–55.
17) Ohne, Y. and K. Narita: Soil Stability (Chapter 7), "Handbook of Soil Engineering", The Japanese Society of Soil Mechanics and Foundation Engineering, 1982, pp. 223–262 (in Japanese).
18) Graham, J.: Method of Stability Analysis (Chapter 6), "Slope Instability", John Wiley & Sons Ltd., 1984, pp. 171–215.

Appendix

1. Monitoring system

The vertical load is measured by load cell (C2), (**Fig. 4**). The sum of the loads on the rubber edge (100 kgf), the friction between the sample and the sides of the upper shear box and the weight of the upper part (dashed in the figure) is measured by load cell (C6). The difference between the values of load cell (C2) and load cell (C6) gives the correct vertical load on the shear plane. Shear force is transmitted through the shear zone from the rotating lower half of the shear box to the upper half of the shear box. The resistance acting on the shear plane is calculated from the measured value in the load cell (C3) retaining the upper half from rotation against the loaded shear stress on the shear plane. The shear torque given by a servo motor is monitored by a torque transducer (C7). The horizontal displacement is monitored by a rotary transducer (C5). The displacement at the location of $(r_1+r_2)/2$ of the

shear plane is used as shear displacement. The vertical deformation of sample was measured by means of a linear transducer (C1) monitoring the displacement of the loading plate.

The data concerning the normal stress (VL 1–VL 2), pore pressure, shear stress, shear resistance, variation of sample height and shear displacement were stored by a personal computer through an A/D converter. The rate of sampling by the personal computer was selective between the ranges of 1/20 Hz to 20 Hz. Simultaneously all data were monitored by a multichannel chart recorder to confirm that the high frequency noises did not interfere the digital data saved by the personal computer.

2. Stress loading system

(1) Normal stress loading system : As shown in **Fig. A–1 a)**, high pressure air (10 kgf/cm^2) is supplied by a compressor. Static and cyclic normal stress are generated by an air piston controlled by an electric servo air valve (electric pneumatic converter) connected to a relay booster. An electric control signal is supplied by a personal computer to the normal stress servo amplifier. The electric servo air valve gives a certain air pressure corresponding to the control signal from the servo amplifier. Feedback signal of the monitored total normal stress on the potential shear surface which is given as the difference of values in two load cells (VL 1–VL 2) is supplied to the servo amplifier.

(2) Shear stress loading system : As shown in **Fig. A–1 b)**, static and cyclic shear stress are generated by a servo motor (Q in **Fig. A–2**) and is controlled by a motor control–board. An electric control signal is supplied by a personal computer to the motor control board through the torque control servo amplifier. The servo motor then gives a certain torque corresponding to the control signal from the computer. Feedback signal from the torque transducer (C7) is given to the torque control servo amplifier.

3. Gap control system

Load cell (C6), (**Fig. A–2**) slightly deforms during rapid shearing and cyclic loading in proportion to the change of side friction of a sample to the upper half of the shear box, and the gap between the two halves will change. However, the gap between the upper ring and the lower ring is maintained automatically by a servo motor (N) using the feedback signal from the high precision gap sensor (C8) with a resolution of 0.002 mm.

To keep the gear of the gap control system below the load cell (C6) and the rotary joint (M) always in the compression position, a dead weight is supplied by an air piston (R). The air control system of the counter dead weight is shown in **Fig. A–1**.

4. Calculation of loaded stress and shear resistance

(1) Normal stress : The normal stress is applied to the sample from the air piston (B in **Fig. 4**) measured by load cell (C2) as VL 1. The sum of the side friction of a sample to the upper half of the shear box, rubber–edge force and counter dead weight is measured by load cell (C6) as VL 2. VL 2 is adjusted to zero value under the state without sample. Therefore, during the tests, the value of VL 2 is the variation of the side friction, and the difference between VL 1 and VL 2 gives the real normal load on the shear plane. Then

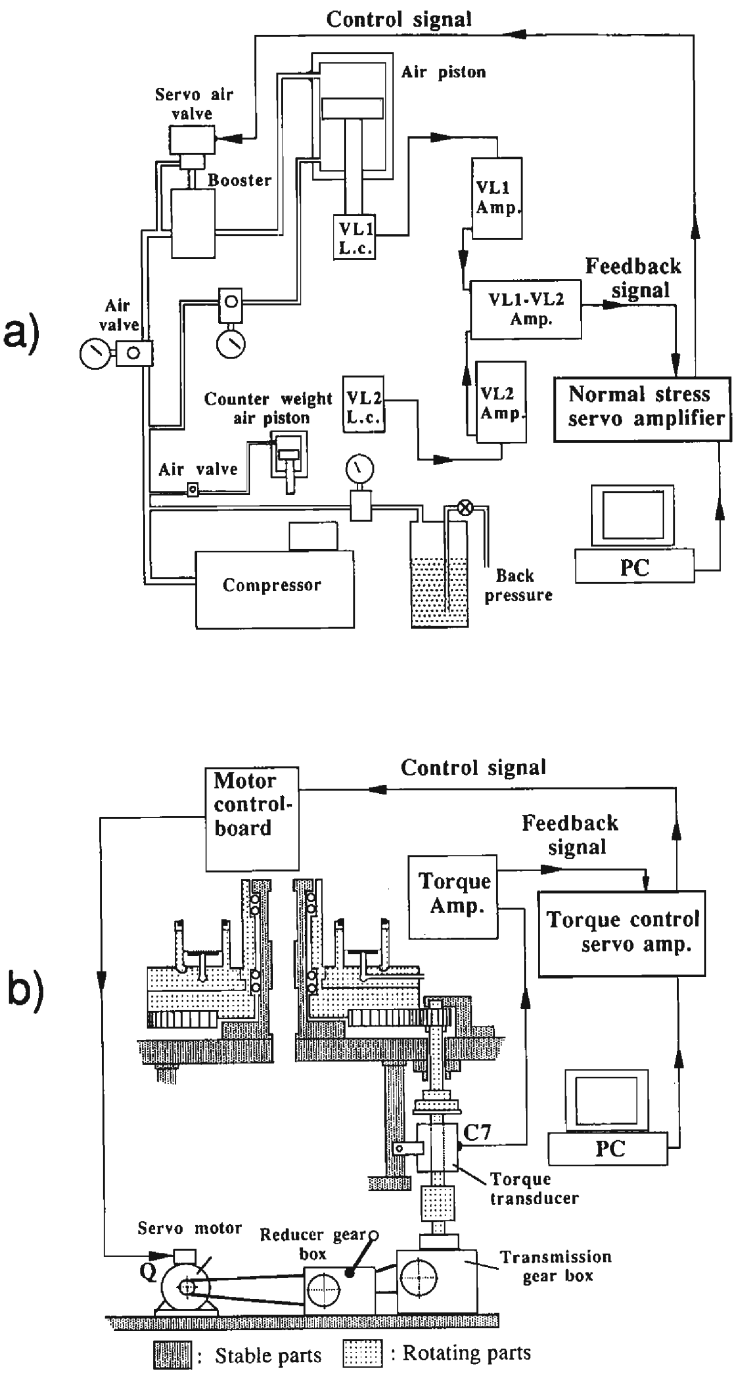

Fig. A–1 Schematic diagram of the air system and the electrical normal stress servo control system a), mechanical and electrical schematic diagram of the torque servo control system b).

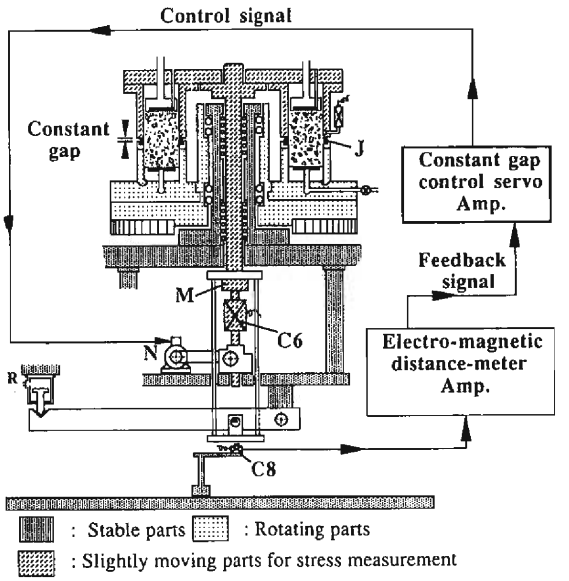

Fig. A–2 Mechanical and electrical schematic diagram of the constant–gap servo control system.

$$F_n = VL_1 - VL_2$$

where F_n: normal load (kgf) on the shear plane. The normal stress on the shear plane is;

$$\sigma = \frac{F_n}{\pi(r_2^2 - r_1^2)} + \gamma t \cdot h$$

where σ: normal stress on the shear plane, γt: unit weight of the sample, h: sample height above the shear plane, r_1: inner radius of the sample box, r_2: outer radius of the sample box.

The maximum value of $(\gamma t \cdot h)$ for the dense sample was about 0.006 kgf/cm^2. In comparison to the normal stress level used in this work (2.0−3.5 kgf/cm^2) this value was almost negligible.

(2) Shear resistance: Expressing the shear resistance due to the friction of the rubber edge as τ_r in terms of shear stress, the shear resistance of the sample as τ and the sum of shear resistance due to the sample and the rubber friction as τ_t, from **Fig. A–3 a)** the shear resistance of a sample can be calculated as follows:

$$F_s \times R = \int_{r_1}^{r_2} 2\pi\tau_t r^2 dr = 2\pi\tau_t \frac{1}{3}(r_2^3 - r_1^3) = \frac{2}{3}\pi(r_2^3 - r_1^3) \times \tau_t$$

where F_s: shear load monitored by the load cell (C3), R: distance between the shear load cell and the axis of the sample box. Then

$$\tau = \tau_t - \tau_r = \frac{3RF_s}{2\pi(r_2^3 - r_1^3)} - \tau_r$$

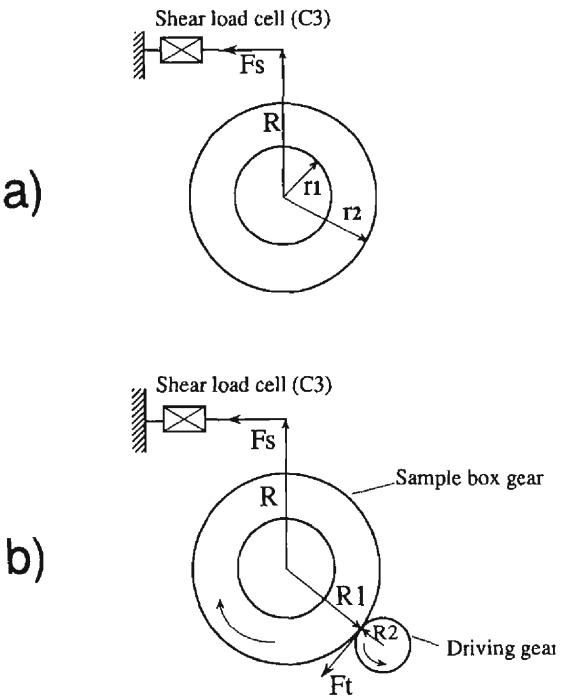

Fig. A–3 Schematic diagram for calculating the shear resistance and the shear stress in the cyclic loading ring shear apparatus.

(3) Shear stress : From **Fig. A–3 b)**, the relations between shear torque (T_M) monitored by torque transducer (C7) in **Fig. 4** and the shear force (F_t) can be calculated as follows :

$$T_M = R_2 \times F_t$$

where R_2 : radius of the driving gear.

Expressing the sum of the shear stress applied to the sample and the rubber edge as τ_T, the shear stress applied to the rubber edge as τ_r and the shear stress applied to the sample as τ_{ts}, then

$$F_t \times R_1 = \int_{r_1}^{r_2} 2\pi\tau_T r^2 dr = 2\pi\tau_T \cdot \frac{1}{3}(r_2^3 - r_1^3) = \frac{2}{3}\pi(r_2^3 - r_1^3) \times \tau_T$$

$$\tau_{ts} = \tau_T - \tau_r = \frac{3R_1F_t}{2\pi(r_2^3 - r_1^3)} - \tau_r$$

where R_1 : distance between the axis of sample box and driving gear.

For each test, before sample setting, the value of the rubber–edge friction (τ_r) was measured. This value was subtracted from the calculated sum shear resistance (τ_t) and sum shear stress (τ_T).